ARL-TR-9858 ● Dec 2023

Scintillator Efficiency and Radiation Damage Mechanisms in Alpha-Photovoltaics

by Jason Barbier, Thomas Bone, Rais Nurhidajat, Mathew Tivey, G Amalthea Trobare, Nusrat Sarwahrdy, Lucas Zhu, Marc Litz, John Derek Demaree, Vijay Parameshwaran, LeighAnn Larkin, Jeremy Smith, Nicholas Barbieri, and Michael Wraback

DISTRIBUTION STATEMENT A. Approved for public release: distribution unlimited.

NOTICES

Disclaimers

The findings in this report are not to be construed as an official Department of the Army position unless so designated by other authorized documents.

Citation of manufacturer's or trade names does not constitute an official endorsement or approval of the use thereof.

Destroy this report when it is no longer needed. Do not return it to the originator.

ARL-TR-9858 ● DEC 2023





Scintillator Efficiency and Radiation Damage Mechanisms in Alpha-Photovoltaics

Jason Barbier, Thomas Bone, Nusrat Sarwahrdy, and Lucas Zhu
University of Maryland, College Park

Rais Nurhidajat
Vanderbilt University

Mathew Tivey
San Diego State University

G Amalthea Trobare
University of Maryland, Baltimore County

Marc Litz, John Derek Demaree, Vijay Parameshwaran, LeighAnn Larkin, and Michael Wraback
DEVCOM Army Research Laboratory

Jeremy Smith and Nicholas Barbieri
General Technical Services, LLC

DISTRIBUTION STATEMENT A. Approved for public release: distribution unlimited.

REPORT DOCUMENTATION PAGE

1. REPORT DATE	2. REPORT TYPE	3. DATES COVERED	
		START DATE	END DATE
December 2023	Technical Report	15 May 2023	15 September 2023

4. TITLE AND SUBTITLE
Scintillator Efficiency and Radiation Damage Mechanisms in Alpha-Photovoltaics

5a. CONTRACT NUMBER	5b. GRANT NUMBER	5c. PROGRAM ELEMENT NUMBER
5d. PROJECT NUMBER	**5e. TASK NUMBER**	**5f. WORK UNIT NUMBER**

6. AUTHOR(S)
Jason Barbier, Thomas Bone, Rais Nurhidajat, Mathew Tivey, G Amalthea Trobare, Nusrat Sarwahrdy, Lucas Zhu, Marc Litz, John Derek Demaree, Vijay Parameshwaran, LeighAnn Larkin, Jeremy Smith, Nicholas Barbieri, and Michael Wraback

7. PERFORMING ORGANIZATION NAME(S) AND ADDRESS(ES)
DEVCOM Army Research Laboratory
ATTN: FCDD-RLA-GC
Adelphi, MD 20783

8. PERFORMING ORGANIZATION REPORT NUMBER
ARL-TR-9858

9. SPONSORING/MONITORING AGENCY NAME(S) AND ADDRESS(ES)	10. SPONSOR/MONITOR'S ACRONYM(S)	11. SPONSOR/MONITOR'S REPORT NUMBER(S)

12. DISTRIBUTION/AVAILABILITY STATEMENT
DISTRIBUTION STATEMENT A. Approved for public release: distribution unlimited.

13. SUPPLEMENTARY NOTES
ORCID IDs: Mark Litz, 0000-0003-0694-4152; John Derek Demaree, 0000-0001-8244-4761

14. ABSTRACT
When used in conjunction with photovoltaics (PVs), scintillators can function as compact alpha-radiation energy converters to form an alpha-photovoltaic (APV). Several materials were evaluated for their suitability as APV scintillators by measuring their luminosity, conversion efficiency, and degradation under alpha-radiation exposure. Conversion efficiency was evaluated by comparing PV output power to incident alpha-radiation power. To assess the luminosity, a PV-based measurement system was designed to quantify the alpha-induced light yield (ph/MeV) and radiation degradation (system efficiency as a function of fluence) of scintillators exposed to a 4.5-MeV alpha-particle beam. The luminosity of single-crystal formats of cesium iodide (CsI) were compared to phosphor powders of strontium aluminate doped with dysprosium and europium; zinc sulfide doped with aluminum, copper, and silver; yttrium aluminum phosphide (YAP:Ce); and yttrium aluminum garnet (YAG:Ce). Scintillator samples were mounted on both indium gallium phosphide (InGaP) and triple-junction PV solar cells. The two PVs were calibrated as a function of optical intensity and emission wavelength. The PV I-V characteristics were measured throughout the alpha-particle exposures to determine the power source efficiency and scintillator luminosity. CsI scintillators affixed to InGaP PV produced the highest alpha-induced luminosity (62.3 kPh/MeV) and required the largest ion fluence (10^{15} ion/cm^2) to reduce the system efficiency to 10% of its beginning of life value.

15. SUBJECT TERMS
scintillator, phosphor, alpha-photovoltaics, ion accelerator, radiation damage, luminosity, material hardness, Electromagnetic Spectrum Sciences, Energy Sciences

16. SECURITY CLASSIFICATION OF:			17. LIMITATION OF ABSTRACT	18. NUMBER OF PAGES
a. REPORT	b. ABSTRACT	C. THIS PAGE		
UNCLASSIFIED	UNCLASSIFIED	UNCLASSIFIED	UU	67

19a. NAME OF RESPONSIBLE PERSON	19b. PHONE NUMBER *(Include area code)*
Marc Litz	(301) 394-5556

STANDARD FORM 298 (REV. 5/2020)
Prescribed by ANSI Std. Z39.18

Contents

List of Figures v

List of Tables vi

Acknowledgments viii

1. Introduction 1

1.1 Scintillator Characteristics 3

1.2 Inorganic Scintillating Mechanisms 4

1.3 Sample Materials 6

2. Modeling and Simulation 6

2.1 SRIM Modeling 6

2.2 MCNP Modeling 7

2.3 Linear Energy Transfer 9

3. Experimental Setup 10

3.1 Scintillator Preparation 11

3.2 InGaP Dicing and Cleaning Process 13

3.3 Photovoltaic Device Preparation 13

3.4 Experimental Configuration 16

4. Results 21

4.1 System Efficiency 21

4.2 Radiation Hardness 24

4.3 Scintillator Luminosity 25

4.4 Powder Scintillator Binder Comparison 26

5. Conclusions and Future Work 26

6. References 28

Appendix A. Scintillator Ranking **32**

Appendix B. Monte Carlo N-Particle (MCNP) Input Cards **49**

List of Symbols, Abbreviations, and Acronyms **55**

Distribution List **57**

List of Figures

Fig. 1 An APV power source 1

Fig. 2 Diagram of the scintillation process (Weber 2002; Lecoq 2007) 5

Fig. 3 Schematic diagram of the energy level and band structure of a single YAG:Ce crystal (Zych et al. 2000) 5

Fig. 4 Penetration depth of a 4.5-MeV α-particle (left), ionization energy by target depth (center), and collision events (right) in ZnS 7

Fig. 5 MCNP geometry specification 8

Fig. 6 MCNP alpha range vs. energy (MeV/cm^3) 8

Fig. 7 a) Electron creation and b) electron energy deposition by depth 9

Fig. 8 a) Alpha energy deposition by depth and b) knock-on electron energy deposition by depth 9

Fig. 9 LET of the alpha particle 10

Fig. 10 a) Average energy deposition of a 4.5 MeV alpha particle by penetration and b) broken up by cell 10

Fig. 11 Surface morphology of $YAlO_3$:Ce scintillator film with a thickness of ca. 80–120 µm in 2.5 wt% PS-at binder. Image was taken with a Keyence optical profilometer at 150× magnification. 12

Fig. 12 SEM images of $SrAl_2O_4$:Dy,Eu (left) and ZnS:Ag (right) films ca. 100 µm thick prepared with 2.5 wt% polystyrene binder at 2000× magnification 12

Fig. 13 Materials stack and I-V curves of the InGaP PV devices (Dai et al. 2017) 12

Fig. 14 Inorganic scintillator films with 2.5 wt% polystyrene binder applied to a triple-junction (TJ) Emcore cell luminescing under exposure to a 385-nm UV lamp 14

Fig. 15 Top side of InGaP cell (left) and bottom side of InGaP cell (right) 14

Fig. 16 Emcore (left) and InGaP (right) PV cells mounted with phosphor scintillators 14

Fig. 17 a) A 25- × 10-mm copper wafer board, b) a two-pin male Molex box connector used on an InGaP device, and c) a two-pin female Molex box connector to BNC connector 15

Fig. 18 Schematic of the pelletron ion accelerator. Experimental schematic (on the bottom right) shows alpha-particle beam exposure of a scintillator mounted on a PV cell. The scintillator is 100 µm thick, which prevents alpha-particle beam penetration into the PV. The IV characteristics of the PV are measured every 60 s throughout exposure. 17

Fig. 19 Raw data collected for CsI on InGaP with I_{PELL} = 350pA (left), and an IV curve and its corresponding PV curve (right) 18

Fig. 20 LED current regulator circuit. The circuit consists of a 9-V battery, a linear voltage regulator, and a 500-ohm potentiometer, which regulates current from 1 to 31 mA 18

Fig. 21 Dark box test assembly consisting of a dual base for InGap and Emcore cells, a filter amount that 4 ND filters, and a changeable lid that fits multiple LEDs 19

Fig. 22 Emcore calibration data using LED diodes with peak wavelength of 655 nm (red), 590 nm (yellow), and 525 nm (green). Optical power from 1 µW to 1.8 mW generates electrical power in the PV from 4 nW to 16 µW. 20

Fig. 23 InGaP calibration data obtained with 655 nm (red), 590 nm (yellow), and 525 nm (green) LEDs. Optical power from 10 nW to 1 mW generates electrical power in the PV from 50 nW to 900 µW. 20

Fig. 24 System efficiency as a function of total ion fluence increases for various scintillators on Emcore PV 22

Fig. 25 System efficiency as a function of total ion fluence increases for various scintillators on InGaP PV 22

Fig. 26 Maximum power point measured on the Emcore PV as a function of total ion fluence, showing the initial value of luminosity as measured by the MPP of the IV curve trace. The degradation of the light yield with increasing ion flux is observed. 23

Fig. 27 Maximum power point measured by InGaP PV as a function of total ion fluence, showing the initial value of luminosity as measured by the MPP of the IV curve trace. The degradation of the light yield with increasing ion flux is observed. 23

Fig. 28 Efficiency degradation during alpha-exposure of CsI:Tl on Emcore PV at I_{PELL} ~1.84 nA 24

Fig. 29 Comparison of ZnS in three binders, all 2.5% by weight. The polystyrene light yield is 40% more luminous than Resin 1. 26

Fig. A-1 Ranked scintillating materials using FOM 37

List of Tables

Table 1 Material characteristics of measured scintillators included in the FOM 4

Table 2 Scintillator material penetration depth, ionization energy, and vacancies per ion. 7

Table 3 System power efficiencies on PVs by scintillator 22

Table 4 The measured PV efficiency, scintillator efficiency MPP, and emission photons from selected scintillators evaluated in this report 26
Table 5 Comparison between electron- and alpha-induced photons 27
Table A-1 Top high-output scintillators 33
Table A-2 Top high-density scintillators 34
Table A-3 Top high-melting-point scintillators 34
Table A-4 Top high molar mass scintillators 34
Table A-5 Least vacancy prone scintillators 35
Table A-6 Characteristics of scintillators that form FOM 36

Acknowledgments

Our team would like to extend gratitude to Dr William A Hollerman of Acadiana Research Laboratory, University of Louisiana at Lafayette, for providing us with sample scintillators to begin the exploration.

The research conducted in this study would not have been possible without the tireless contributions of US Army Combat Capabilities Development Command Army Research Laboratory scientists and support staff. It is dedicated to the Soldiers of the US Army and their families.

1. Introduction

Alpha-photovoltaics (APVs) are high-energy-density sources that a provide low-power output over an extended period of time and can be packaged in a small form factor that can be used to create compact, long-lasting, reliable, and maintenance-free power sources. They can fit on a wide variety of small electrical devices that can be powered for years, depending on the half-life of the radioisotope used. Potential applications include powering medical devices, tracking and tagging sensors, unmanned autonomous vehicle subsystems, and other critical military equipment. Integration of these devices can enhance the overall readiness of Soldiers and their equipment. While more energetic than beta-particles (electrons), alpha-particles also cause more damage to surrounding materials (Hong et al. 2014; Russo et al. 2017; Berman et al. 2018; Tyagi et al. 2021). Scintillators used in APVs will therefore need to be resistant to alpha-radiation-induced damage. In this investigation, we evaluate several scintillator materials for their use in APVs by quantifying their efficiency and operational lifetime.

Scintillators are materials that absorb energy through charge particle excitation and release it in the form of electromagnetic (EM) waves in the visible, infrared (IR), and ultraviolet (UV) portions of the EM spectrum. When this light is absorbed by a photovoltaic (PV) device, it is converted into electrical power (Fig. 1). The scintillator layer acts as a protective barrier from the alpha particles that damage the semiconductor (Cao and Xue 2014). A schematic design is shown in Fig. 1, where a radioisotope emitter is deposited in between two layers of phosphor, each surrounded by a PV, generating electrical current. Alpha particles are typically more energetic than beta particles or gamma rays and deliver their energy to materials over a short range (~20 μm) as dictated by linear energy transfer (LET).

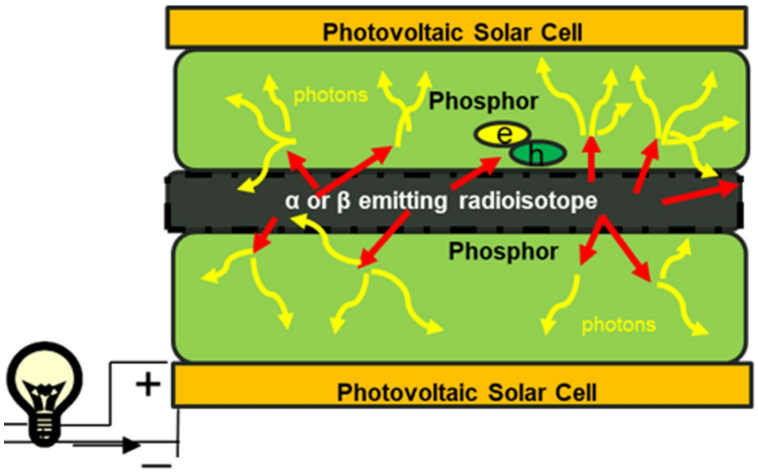


Fig. 1 An APV power source

The effectiveness of voltaic systems utilizing alpha particles as an energy source is limited by radiation damage that rapidly degrades the performance of these devices. Alpha particles damage materials (Xu et al. 2018) whose crystal structures require low defect levels for efficient operation (Cress et al. 2008; Xue et al. 2019). Early alpha radio voltaics made use of silicon (Si) and germanium (Ge) to convert radiation into electrical current (Pfann and Van Roosbroeck 1954). Early silicon carbide (SiC) APV devices using americium-241 (^{241}Am) as an alpha particle emitting radioisotope showed a rapid degradation of the SiC diode structure to 58% of initial power over 100 h (Rybicki et al. 1996). Structures using InGaP PV materials were developed with limited success. In previous experiments the measured short circuit current degraded to 45% of its beginning-of-life value after 264 h of exposure to 1/2 mCi ^{210}Po (Bailey et al. 2005; Cress et al. 2006). An APV architecture provides a method of mitigating radiation damage by using a scintillator as a protective barrier that protects the PV layer from direct exposure to alpha radiation.

A literature review was performed to obtain the scintillator properties most relevant to radioisotope power source applications (Zorn 1990; Colerico et al. 1995; Yamaguchi et al. 1999; Wu et al. 2003). Modeling of alpha particle interaction with each scintillator was conducted using Stopping and Range of Ions in Matter (SRIM) (Ziegler et al. 2010) and Monte Carlo N-Particle (MCNP) (Werner et al. 2018) software. A combination of the material properties and modeling was used to create a figure of merit (FOM) to determine which scintillators would produce the highest luminescent intensity and the least material degradation. These materials, along with scintillators previously evaluated for effects of proton luminosity and damage (Holland et al. 1991; Hollerman et al. 1991), were chosen to undergo experimental investigation to evaluate their power output, efficiency, and lifetime to determine the best scintillators for APVs. The scintillators were irradiated with 4.5-MeV alphas using a pelletron ion accelerator at Aberdeen Proving Ground (APG), Maryland. The irradiated scintillators were then subjected to additional experiments to measure the power output and efficiency.

The objective of this report was to measure scintillator light output and luminosity for alpha efficiency, explored in Section 4.3. Section 1 contains a summary of the scintillator literature and our selection process for those scintillators chosen for experimentation. The modeling of alpha particle interactions is described in Section 2. The experimental setup is described in Section 3. Our results are documented in Section 4. Intended future research is described in Section 5. This work summarizes the effort of a team of interns to understand, design, and measure the alpha particle–induced luminosity of scintillators as applied to radioisotope power source applications.

1.1 Scintillator Characteristics

Scintillators are materials that emit light when subjected to external sources of energy. Photoluminescence is EM generation sourced by light. Triboluminescence is EM generation sourced by pressure (Hollerman et al. 2003). Chemiluminescence is sourced by chemical reactions (Tzani et al. 2021). Electroluminescence is sourced by high electric fields (Chase et al. 1969). Radioluminescence is sourced by radioisotope decay products. Ionizing radiation (i.e., gamma, electron, alpha) generates optical power in luminescent materials. Scintillating materials (and phosphors) are found in commercial applications of LED and fluorescent lighting, displays, medical image amplifiers, and radiation detection (Yen et al. 2019).

Using scintillators to detect radiation has a long history (Gektin and Korzhik 2017). In the 1950s, anthracene radiation damage was measured. The luminescent efficiency was fit to an equation of the form $1/(1 + AN)$, where N was the fluence of particles and A is a constant (Birks and Black 1951). A goal of our research was to test an array of scintillators to get a better value for A for the case of APV.

Scintillators of interest for this investigation were ranked by luminosity and radiation hardness for use in an APV power source. The properties of scintillators deemed most relevant to the development of APVs were luminescent energy conversion efficiency and radiation hardness. Luminescent efficiency was quantified as light yield in numbers of photons per incident particle energy, given in units of photons/MeV. Radiation hardness was quantified as change in the power output of material as a function of ion fluence. Radiation hardness was expected to depend on density, atomic mass, melting point, and vacancies created per ion (Ziegler et al. 2010). Alpha particles displace atoms in the scintillator's lattice to create Frenkel pairs that reduce the scintillator conversion efficiency. Alpha particles are more energetic than beta particles but are also more damaging to surrounding materials. This makes radiation-resistant scintillators essential for continuous operation over the useful lifetime of alpha radioisotope's source.

To evaluate common scintillators, we created a FOM based on scintillator characteristics given in Table 1. A good scintillator requires a large density (ρ, g/cm^3), a large melting point (T_{MP}, °C), a high atomic weight (AMU), low vacancy formation rate (vacancies/ion), and a large conversion efficiency (L_{int}, photons/MeV) to obtain the desired radiation resistance and power output. A high-density scintillator will convert more incident radiation to light. A large atomic mass will reduce displacement of lattice ions caused by alpha-lattice collisions. A high melting point reflects the material's ability to maintain a stable structure under conditions of high heat density and capacity to contain the heat/stress of energy deposition. A low-vacancy formation rate reduces the number of displacement

events and thus minimizes the defect formation in crystals. These parameters are used to measure optical power generation, mechanical strength, thermal stability, ballistic cross section, and damage production.

$$FOM \propto \frac{L_{int} \times \rho \times T_{MP} \times AMU}{\frac{vacancies}{ion}} \quad (1)$$

The material properties of 66 scintillators relevant to the development of APVs were compiled over the course of our investigation. A complete summary of these properties is presented in Appendix A. An abridged summary is provided in Table 1.

Table 1 Material characteristics of measured scintillators included in the FOM

Scintillator	Wavelength (nm)	Intensity (kph/MeV)	Density (g/cc)	Melting point (°C)	Mass (AMU)	Vacancy per ion	FOM
CsI:Tl	550	54	4.51	894	260	139.4	419326
Gd_2O_2S:Pr	510	9	7.32	1050	379	144.1	181724
$SrAl_2O_4$:Eu,Dy	522	46	3.56	1200	206	125.2	322676
YAG:Ce	560	15	5.37	1970	594	126.4	632823
YAG:Eu	545	25	5.37	1875	594	129.2	632823
YAG:Tb	580	25	5.37	1875	594	129.2	632832
YAP:Ce	378	25	4.57	1875	164	129.2	319296
Y2O2S:Eu	615	2.1	2.88	2350	242	135.3	25408
Y2O2S:Tb	530	2.1	2.88	2350	242	135.3	25408
ZnS:Ag	450	52.2	4.09	1850	97	159.7	147304

1.2 Inorganic Scintillating Mechanisms

The details of scintillation are illustrated in Fig. 2 (Weber 2002; Lecoq 2007). Scintillation begins with the absorption of incident-ionizing radiation and subsequent creation of a primary electron–hole pair. The primary electron generates additional electron–hole pairs through radiative decay, nonradiative decay, and inelastic electron–electron scattering during propagation (Bizzari 2010). Once the energy of the electron–hole pair falls below the ionization energy, electrons thermalize to the bottom of the conduction band and holes thermalize to the top of the valence band. The electron–hole pairs will either remain free or combine to form excitons. This is followed by a transfer of energy from the electron–hole pairs to the luminescent center forming excitonic states and groups of excited luminescent centers. Finally, the luminescent centers relax, with electron–hole pairs undergoing radiative recombination and producing light. The wavelength of emission, quantum yield, and luminosity of this process depends on the specific scintillator used.

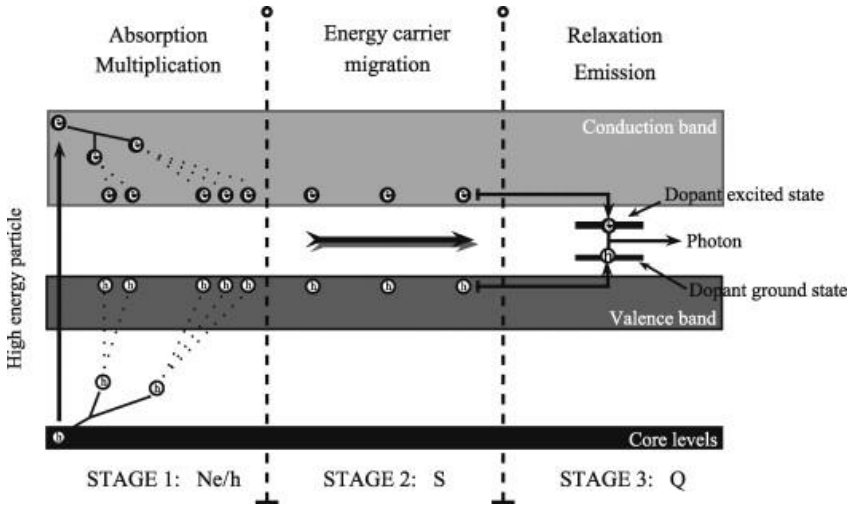


Fig. 2 Diagram of the scintillation process (Weber 2002; Lecoq 2007)

For a material to be a scintillator, it must include luminescent centers. The properties of the luminescent centers define the scintillator type. Intrinsic (undoped) scintillators include excitonic (CsI), self-activated (CdWO4), and semiconductors (CuI). Extrinsic (doped) scintillators are one of two kinds of doped materials: activated (CsI:Ce) or doped semiconductors (CdS:Te). Core-valence luminescence scintillators are characterized by a core-valence bandgap energy that is less than that of the valence-conduction bandgap (Weber 2002; Lecoq 2007; Kumar and Luo 2021).

Most scintillators surveyed in this project are extrinsic scintillators. One example of an extrinsic scintillator is YAG:Ce. An energy level schematic of the host YAG lattice and Ce3+ ion is shown in Fig. 3 (Zych et al. 2000).

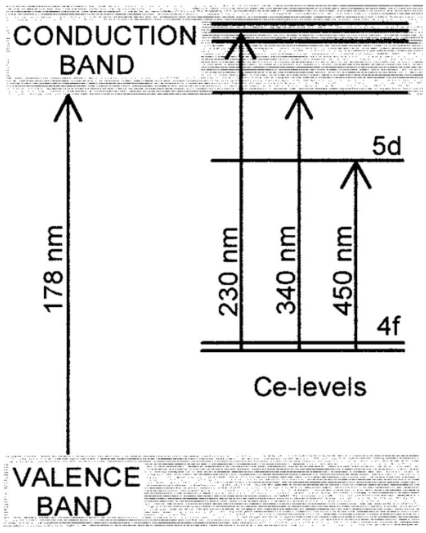


Fig. 3 Schematic diagram of the energy level and band structure of a single YAG:Ce crystal (Zych et al. 2000)

1.3 Sample Materials

Sixty-six scintillating materials were investigated through a literature review and are tabulated in Appendix A. Scintillator properties were documented and ranked, resulting in a FOM based on light yield and radiation tolerance as described in Eq. 1. Those scintillators that scored a high FOM and were readily available were identified for experimental exploration. Density, atomic mass, and melting point were determined by looking up already-defined material properties, while the vacancy creation rates were calculated (more details provided in Section 2.1). A summary of the scintillators used in this investigation is provided in Table 1.

2. Modeling and Simulation

Modeling tools provide scientific insight into the mechanisms of energy transfer for alpha particle propagation in scintillator materials (Guthoff et al. 2014; Nordlund 2019; Yost et al. 2019). Numerical simulations were used to assess scintillator properties such as penetration depth and vacancies per ion. This helped inform decisions on material choice and thickness for experimentation. The alpha interactions can be described by ionization energy loss (transfer of alpha kinetic energy to the electron cloud) and nonionizing energy loss (ballistic displacement of atoms in materials). The modeling discussed in this section provides insight into these energy loss mechanisms.

2.1 SRIM Modeling

Stopping and Range of Ions in Matter (SRIM) models ion transport through material in two dimensions. SRIM was used to model the penetration depth, ionization energy, and vacancies per ion for 4.5-MeV alpha particles in a variety of scintillators as shown in Table 2. This allowed us to determine the necessary thickness of the scintillator material to ensure all alpha radiation energy was captured, since peak ionization occurs at approximately 90% of the penetration depth (Fig. 4, center). The number of vacancies per ion created represents the number of atoms displaced in the crystalline structure per incident ion. It is a measure of the damage done to the scintillator material by the alpha particle.

SRIM modeling was completed using the Kinchin–Pease quick calculation in the SRIM-2008 software version with 5,000 ions simulated. The Kinchin–Pease model analytically determines the number of point defects generated from the source ion during a primary recoil. A primary recoil is created by the direct collision of an ion with an atom in the target material as opposed to a secondary recoil, which is generated from subsequent recoils. The accuracy of the Kinchin–Pease model

yields a higher uncertainty when compared to the Norgett, Robinson, and Torrens (NRT) and molecular dynamics (MD) models (Stoller et al. 2013). For the purposes of this research, only the relative values of the vacancies per ion were used as a metric for comparison between several scintillators.

Table 2 Scintillator material penetration depth, ionization energy, and vacancies per ion.

Scintillator	Density (g/cc)	Penetration depth (μm)	Peak ionization energy (eV/angstrom-ion @ μm)	Vacancies per ion
CsI	4.51	21.5	30.3 @ 19.5	134.9
ZnS	2.50	25.7	24.6 @ 23.1	159.7
$SrAl_2O_4$	3.56	15.3	43.9 @ 13.6	125.2
YAP	5.37	10.7	61.9 @ 9.3	126.4
YAG	4.57	12.0	55.4 @ 10.5	126.4
Y_2O_2S	2.88	13.6	49.8 @ 12.2	135.3
LuAG	6.73	10.9	59.0 @ 9.6	140.1
Gd_2O_2S	7.32	11.9	52.4 @ 10.6	144.1
GAGG	6.63	10.9	56.1 @ 9.5	144.6
BGO	7.13	12.8	47.9 @ 11.2	170.3
LYSO	7.40	11.4	56.2 @ 10.1	163.3

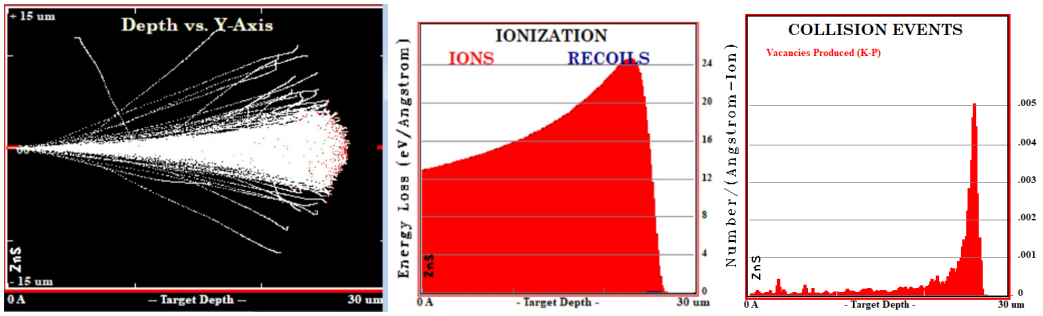


Fig. 4 Penetration depth of a 4.5-MeV α-particle (left), ionization energy by target depth (center), and collision events (right) in ZnS

2.2 MCNP Modeling

Monte Carlo N-Particle (MCNP) is a software application that allows for the 3D modeling of alpha particle energy deposition and particle flux in the scintillator. The geometry of the problem was constructed in MCNP as shown in Fig. 5. The ZnS was separated into 15 layers, each 3 μm deep. Layers are also referred to as cells. The ZnS was then encased in a layer of InGaP PV (layer 16), which in turn was surrounded by air (layer 17). Layer 18 is an InGaP shield, layers 31 and 32 are an air casing, and layers 34 and 35 are the outside world. The full input deck is shown in Appendix B for completeness.

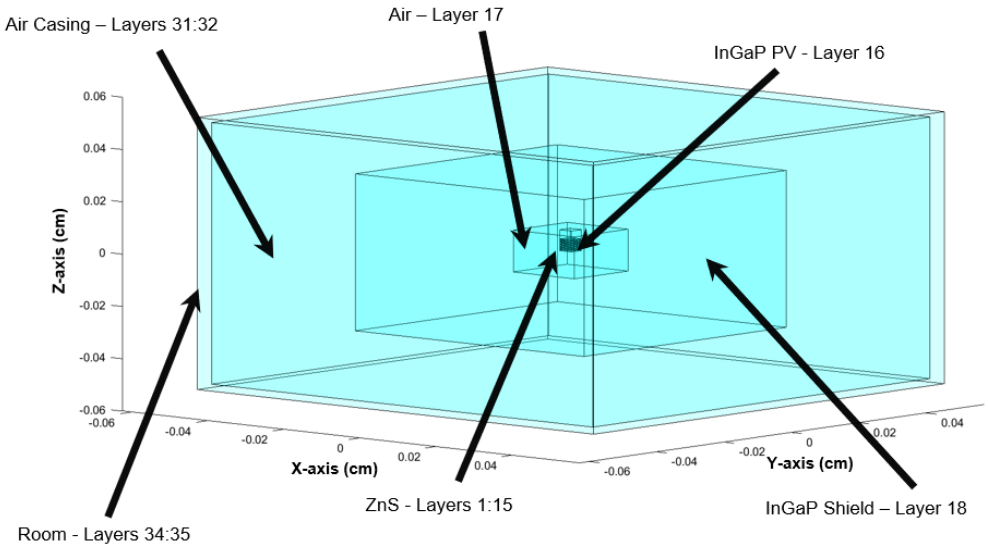


Fig. 5 MCNP geometry specification

The simulation was run with a 4.5-MeV alpha particle point source. The alpha energy deposition in ZnS is shown in Fig. 6. Here, zero is the start of the sample, and negative distances indicate a reflected particle. The data shows that 4.1 MeV of the original 4.5 MeV was absorbed by the scintillator, 397 keV of energy was transferred to electrons, and less than 1 eV was emitted as light. Figure 7 shows that 5,800 electrons were created for each sourced alpha particle. Figure 8 compares alpha energy deposition (a) to electron energy deposition (b) in the ZnS layers. Figure 8b represents the profile of energetic electrons created by the alpha particle through ionizing events. These figures demonstrate that alpha energy absorption peaks at approximately 25 μm while electron energy absorption peaks at the surface. Ninety percent of the energy transported by the electrons is absorbed within the first 20 μm of material.

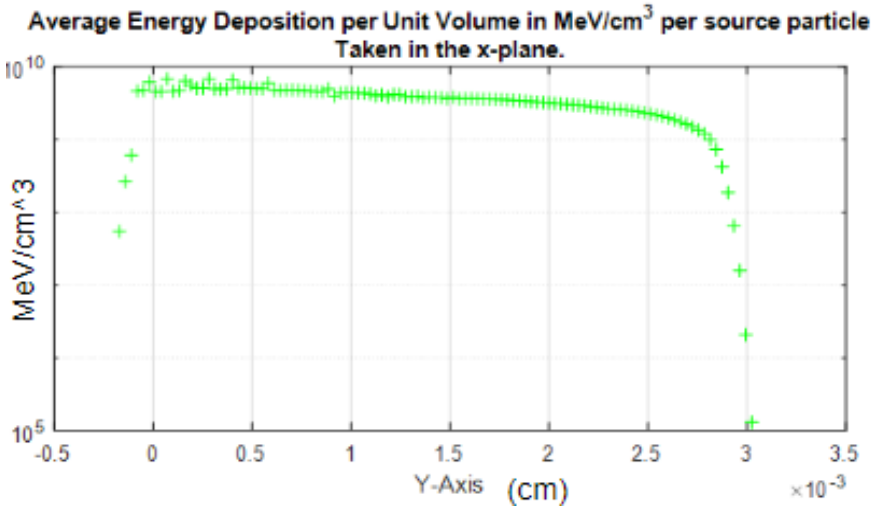
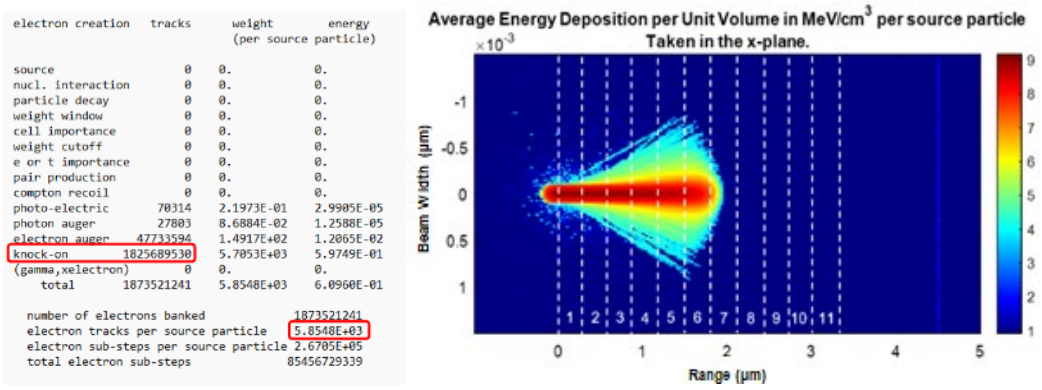
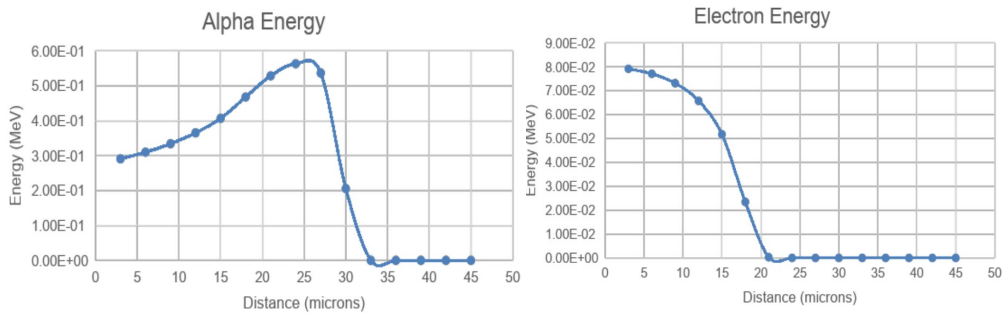


Fig. 6 MCNP alpha range vs. energy (MeV/cm^3)



a) b)

Fig. 7 a) Electron creation and b) electron energy deposition by depth



a) b)

Fig. 8 a) Alpha energy deposition by depth and b) knock-on electron energy deposition by depth

2.3 Linear Energy Transfer

Linear energy transfer (LET) describes the process by which an ionizing energy particle, such as an alpha, loses its energy to the irradiated material. It is a measure of the average EM energy loss as a charged particle moves through the target material per unit length. LET will slow alpha particles until they deposit their remaining kinetic energy into the scintillator (Fig. 9). This final deposition of energy comes in the form of ballistic collisions of ions with atoms in the scintillator, which causes radiation damage through displacement (nonionizing energy loss).

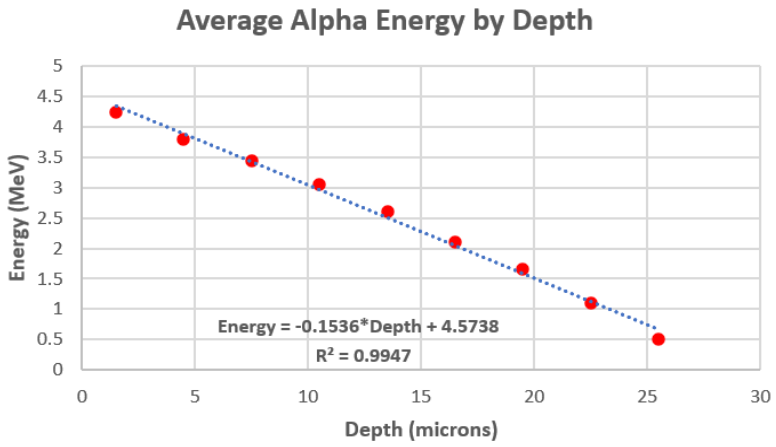
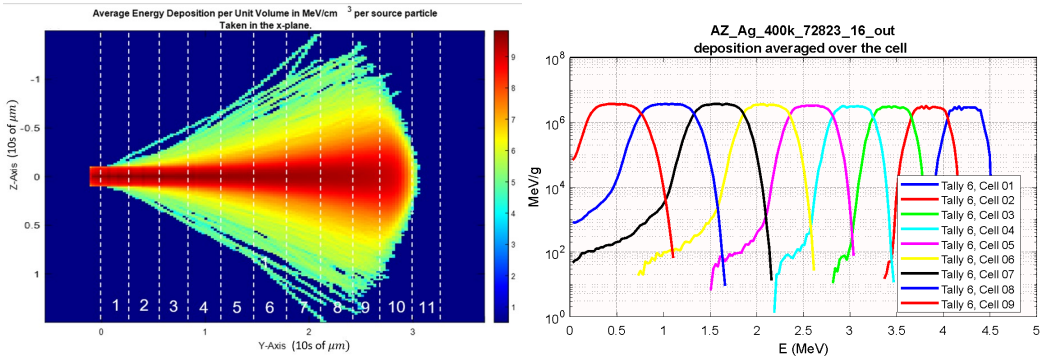


Fig. 9 LET of the alpha particle

An alpha particle's kinetic energy decreases linearly as it travels through the scintillator. LET has been illustrated in Fig. 10 for helium ions in ZnS polycrystalline (powder) form. This allowed us to better understand how alpha particles transfer energy into ionization processes within the scintillator that creates luminescence. One observation taken from Fig. 10 is that the low-energy tail of alpha-induced energy deposition broadens as alphas penetrate deeper into the ZnS. This indicates that a greater percentage of the remaining alphas have lost their energy to ionization processes.



a) b)

Fig. 10 a) Average energy deposition of a 4.5 MeV alpha particle by penetration and b) broken up by cell

3. Experimental Setup

In order to test for luminosity and radiation tolerance, a select number of scintillating materials were chosen based on the numerical modeling described in Section 2, the FOM proposed by Eq. 1, and similar research done with electrons (Yen et al. 2019). Polycrystalline scintillator powers were sourced from several chemical manufactures and applied as thin films using several binders for testing, as described in Section 3.1. The PVs were prepared and integrated with the

scintillator thin films as described in Sections 3.2 and 3.3. The films were then characterized by their output luminosity and lifetime as described in Section 3.4.

3.1 Scintillator Preparation

Two solutions of binder in toluene were prepared: 2.5 wt% atactic polystyrene (PS-at) and 5.0 wt% Norland Optical Adhesive 63 (Resin 1), a urethane-based UV cure resin purchased from Newport. Suspensions of the various polycrystalline scintillator powders in binder solutions were prepared such that the final composition of each binder was 2.5 wt% following the evaporation of any toluene. Aliquots of 32 or 24 μL of the PS-at or UV resin suspensions, respectively, were applied with a micropipette to 10- × 10- × 0.2-mm sodium borosilicate glass slides. The slides were then agitated to spread the solution evenly. The slides were left under ambient hood conditions for several minutes to allow the toluene to fully evaporate. The UV binder then needed an additional resin cure under 385 nm of light for at least 2 min. All scintillator films surveyed in this investigation were prepared using this procedure.

Each film was analyzed using a Keyence FHX optical profilometer to ensure an average thickness of 100 μm, not to exceed 60–130 μm, in order to ensure the film is thicker than the stopping distance of a 4.5-MeV alpha beam (Fig. 11). The uniformity and grain size of each film were measured using a scanning electron microscope (SEM) (Fig. 12). The scintillators chosen for investigating binder transparency and radiation tolerance were strontium aluminate doped with dysprosium and europium ($SrAl_2O_4$:Dy,Eu) and zinc sulfide doped with silver (ZnS:Ag), possessing grain sizes of 5–15 and 1–5 μm, respectively. The glass slides were then applied to PV (Emcore, see Fig. 13 and InGaP) cells using a UV cure resin (Section 3.3) and irradiated using the pelletron ion accelerator (Section 3.4). Two sets of five scintillators (YAG:Eu, Y_2O_2S:Eu, Gd_2O_2S:Pr, Y_2O_2S:Eu, ZnS:Ag) were then prepared using the 2.5 wt% PS-at solution to compare the effect of applying the films directly to InGaP with the indirect application to glass slides.

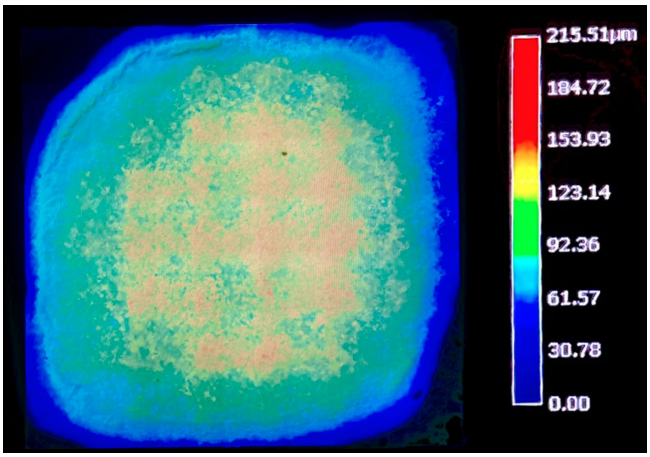


Fig. 11 Surface morphology of $YAlO_3$:Ce scintillator film with a thickness of ca. 80–120 µm in 2.5 wt% PS-at binder. Image was taken with a Keyence optical profilometer at 150× magnification.

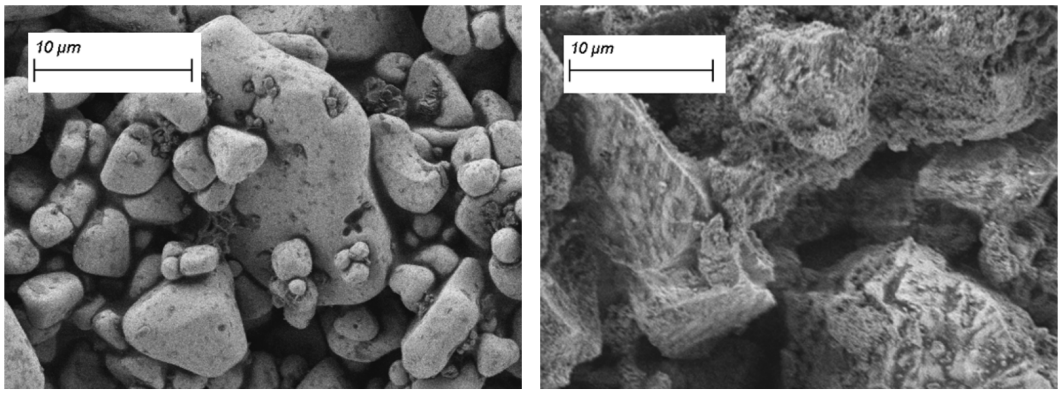


Fig. 12 SEM images of $SrAl_2O_4$:Dy,Eu (left) and ZnS:Ag (right) films ca. 100 µm thick prepared with 2.5 wt% polystyrene binder at 2000× magnification

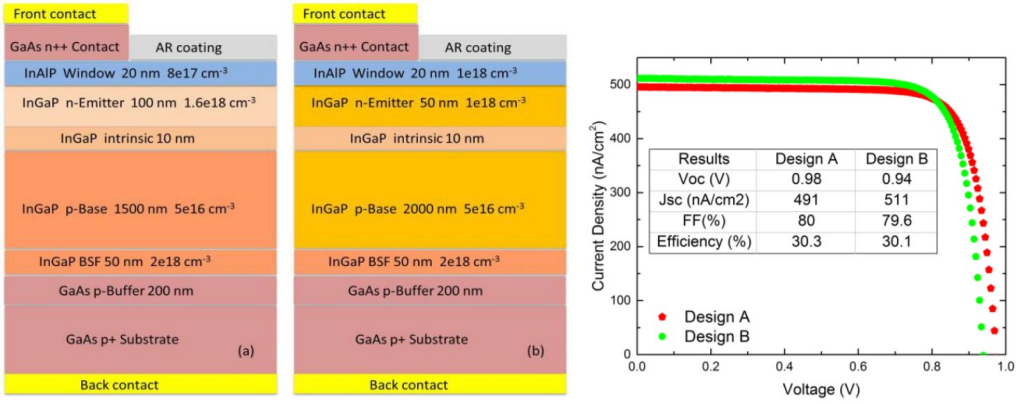


Fig. 13 Materials stack and I-V curves of the InGaP PV devices (Dai et al. 2017)

3.2 InGaP Dicing and Cleaning Process

A 6-inch-diameter wafer of InGaP (grown by MicroLink Devices, Inc) was diced into 1 cm^2 square cells. Figure 13 shows the materials stack of the InGaP cell and representative I-V curves of the cell under 1.27 $\mu W/cm^2$ monochromated light at a wavelength of 600 nm (Dai et al. 2017). An automated dicing machine was configured to dice the wafer at specified horizontal and vertical intervals. After the dicing process, the InGaP cells needed to be cleaned individually to remove debris and other waste from the wet cutting saw of the dicing machine. The cleaning process involved separating the wafer into 112 individual InGaP cells and placing each cell in an acetone solution in a watch glass, wiping the top and bottom surfaces, then moving to an isopropyl alcohol (IPA) solution and wiping a second time. Each cell was in the baths for 1 min. The acetone removes stray metals and debris. The IPA washes away the film produced from the acetone. Finally, the wet InGaP cells were placed on a lint-free cleanroom wipe (Kimtech) for 2 min to dry. To speed up the process, it is recommended to have multiple workbenches to distribute the workload. A batch of cells can be placed in the solution as long as they do not scratch each other. Once cleaned, the cells are placed in a container for packaging on a printed circuit board (PCB).

3.3 Photovoltaic Device Preparation

Two types of PV cells were prepared for these experiments: triple-junction InGaP/GaAs/Ge Emcore solar cells shown in Fig. 14 (Stan et al. 2000) and single-junction InGaP PV devices shown in Fig. 15 (Dai et al. 2017). The larger-size Emcore cells (2 × 3 inches) were used to fit multiple scintillator samples on the PV for rapid evaluation. The Emcore PV is less sensitive to light and cannot provide as precise data as the InGaP PV, as it requires a minimum of 100 nW of optical power (Fig. 16). This requires a pelletron current of at least 2 nA to generate measurable scintillator emissions. The Emcore devices were evaluated first to determine which scintillators yield the best system efficiency and radiation hardness. The InGaP devices were then used to collect more precise data to assess the luminosity of the scintillators of interest.

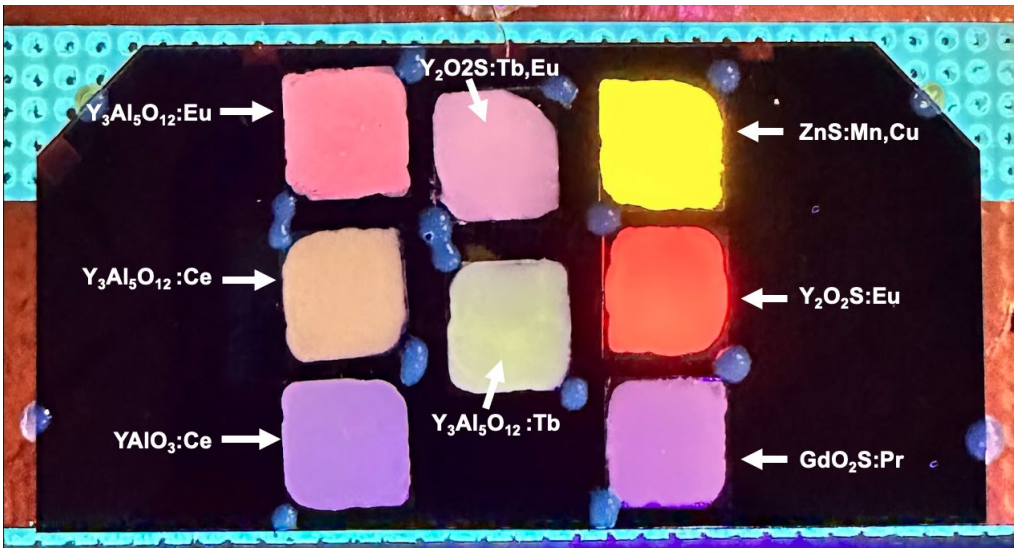


Fig. 14 Inorganic scintillator films with 2.5 wt% polystyrene binder applied to a triple-junction (TJ) Emcore cell luminescing under exposure to a 385-nm UV lamp

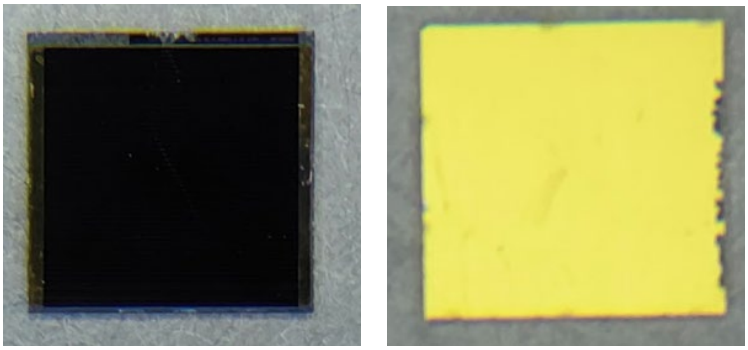


Fig. 15 Top side of InGaP cell (left) and bottom side of InGaP cell (right)

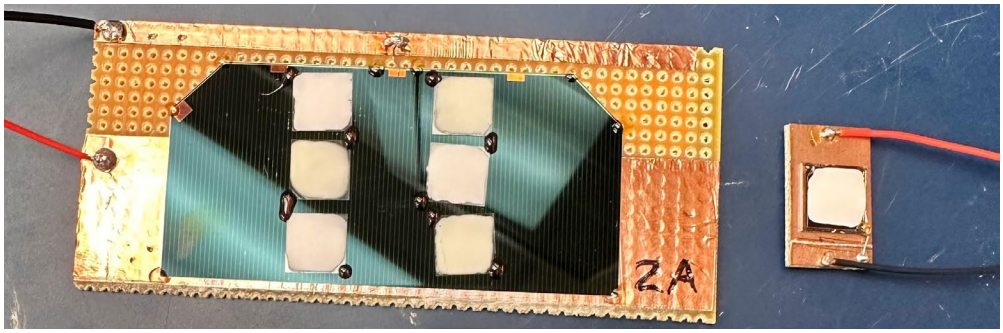


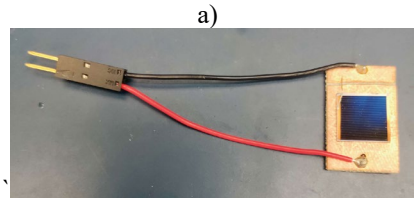
Fig. 16 Emcore (left) and InGaP (right) PV cells mounted with phosphor scintillators

Powder phosphor samples were prepared on glass slides. Single-crystal scintillators were mounted on the PV devices using UV cure epoxy to secure them in place. Powder phosphor samples were also applied directly to the InGaP PVs to investigate the impact of the glass slides on the results.

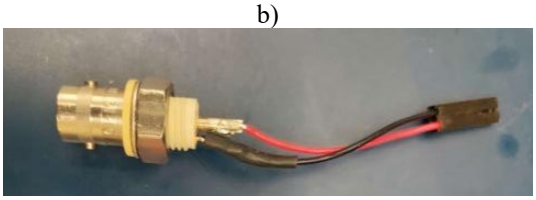
The triple-junction Emcore cell was incorporated into a testing mount by using an electrically conductive silver epoxy (Epo-Tek P1011) to fix the bottom positive contact to a copper substrate. To prevent thermally induced damage to the device, heat was not used to cure the epoxy. UV-cure epoxy was used to hold the Emcore PV cell in place while the silver epoxy cured. The base of the substrate was constructed with a 50- × 100-mm piece of insulating perforated board containing two separate pieces of conductive copper tape. The two strips of copper tape provide electrical contacts to access the cathode and anode of the Emcore PV cell. The cathode was wire bonded to one section of copper tape, as shown in Fig. 16. Wire leads from a two-pin Molex box connector were then soldered to both contacts to complete the device (referenced on Fig. 17b). This two-pin connector directly interfaces with a BNC cable (Fig. 17c) used to switch between the Emcore and InGaP devices.



a)



b)



c)

Fig. 17 a) A 25- × 10-mm copper wafer board, b) a two-pin male Molex box connector used on an InGaP device, and c) a two-pin female Molex box connector to BNC connector

The InGaP devices were mounted to 25- × 10-mm sections of copper wafer board using the same procedure. The wafer board is constructed of two thin sheets of copper sandwiching fiberglass. The board was separated into two isolated conductive sections to be used as electrical contacts for the InGaP cell by etching a line through one of the copper layers. A continuity tester was used to validate the electrical isolation of the contacts. The wafer board is shown in Fig. 17a. Since the

InGaP cell can be heated to 150 °C without damage, the electrically conductive silver epoxy was heated first to 90 °C for 30 min then 150 °C for 90 min to fully cure the epoxy. Wire leads from a two-pin Molex box connector were then soldered onto the two sections of copper wafer board to complete the device.

Since both the triple-junction Emcore PV and InGaP cells are brittle and thin, physical and electrical damage can easily occur during handling. These cells are susceptible to hairline cracks and chipping along the edges, and also thermal damage caused by the soldering or baking process. To determine what steps of the fabrication process damaged the PV cells, an IV curve tracer and a voltmeter were used to monitor the performance of the PV cells after each step. Three causes of PV cell damage were identified:

- Excessive silver epoxy use, which resulted in spillage onto the chip corners
- Damage from excess localized pressure during the wire bonding process
- Damage from applied heat during baking and soldering

Wire bonding was the most frequent cause of cell damage. While no physical damage was observed during this process, IV curve and voltmeter measurements often measured reduced voltage or no voltage from the processed cells. Ultrasonic waves used to melt aluminum wire during wire bonding are suspected to have been the cause of internal damage to the PV cells.

3.4 Experimental Configuration

Scintillators were exposed to a beam of 4.5-MeV helium ions (to simulate alpha radiation exposure) using a National Electrostatics 5SDH-2 positive ion accelerator (a "pelletron") at APG. Using an RF plasma source and a rubidium vapor, a He^- beam was injected into an evacuated acceleration tube, where the negative ions underwent electrostatic acceleration toward a high-voltage terminal (~1.5 MV). As these negatively charged ions reached the high-voltage terminal, with energies of approximately 1.5 MeV, they passed through a small region of slightly higher-pressure nitrogen gas (a "stripper canal"), where they underwent electron loss via collisions with gas atoms. A fraction of these ions will lose three electrons, resulting in an approximate 1.5-MeV beam of doubly charged He++ ions, which was then accelerated further toward ground potential, gaining an additional approximate 3.0 MeV of energy (the product of the electrostatic potential and the electronic charge on the ions). At the exit of the accelerator, the helium beam had roughly 4.5 MeV of energy (1.5-MeV acceleration up to the terminal, and 3.0-MeV accelerator back down to ground), although some experiments were done with a final energy of 4.2 MeV to achieve better beam energy stability. A diagram of the pelletron is shown

in Fig. 18. The helium ions were then focused onto various scintillator materials, where some of their kinetic energy was converted into light. The light emitted from the scintillator was converted into electrical energy by the PV cell mounted underneath the scintillator. An HP 6250 source meter controlled by a Raspberry Pi microprocessor was used to record the IV trace from the PV diode to monitor real-time performance of the system during the exposures. The current and voltage output of the PV was measured throughout the experiments.

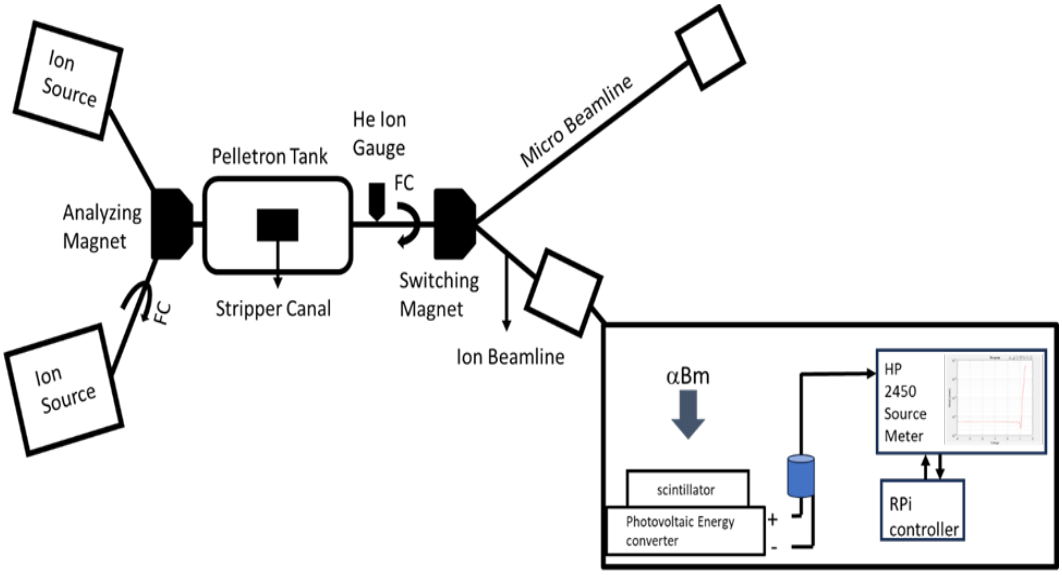


Fig. 18 Schematic of the pelletron ion accelerator. Experimental schematic (on the bottom right) shows alpha-particle beam exposure of a scintillator mounted on a PV cell. The scintillator is 100 µm thick, which prevents alpha-particle beam penetration into the PV. The IV characteristics of the PV are measured every 60 s throughout exposure.

Data analysis provided the open-circuit voltage (V_{OC}), short-circuit current (I_{SC}), maximum power point (MPP), fill factor (FF), and series resistance (R_{SER}) for each IV curve cycle. This data was combined with the corresponding pelletron current (I_{PELL}) and voltage (V_{PELL}) to calculate the total ion fluence, system efficiency (η_{system}), and radiation degradation during ion exposure. Ion fluence was calculated by converting the pelletron current to ion rate (ion/s) and integrating over time. Maximum power point (MPP) shown in Fig. 19 (right) was calculated by multiplying the current and voltage between V = 0 and V_{OC}, then finding the voltage location at which the maximum was located. The MPP was then used to calculate the fill factor by dividing it by the product of the short-circuit current and open-circuit voltage using Eq. 4. The efficiency of the system was calculated by dividing the maximum power point (power out) by the pelletron power (power in). Pelletron power was calculated by multiplying the pelletron current and voltage.

$$Fluence\ (ions) = [\ I_{PELL} / (\ 2 \times 6.25 \times 10^{18} C\ )\ ] \times Seconds \qquad (2)$$

$$MPP = (IMPP \times VMPP) \quad (3)$$

$$FF = MPP / (ISC \times VOC) \quad (4)$$

$$\eta system = MPP / (IPELL \times VPELL) \quad (5)$$

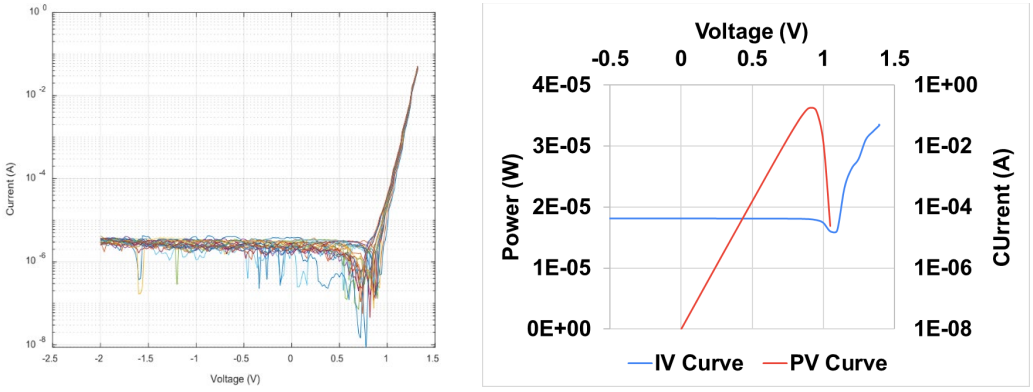


Fig. 19 Raw data collected for CsI on InGaP with I_{PELL} = 350pA (left), and an IV curve and its corresponding PV curve (right)

The PVs were optically calibrated using several LEDs. The LEDs were selected for emission wavelengths (655, 590, and 525 nm) that aligned with the range of peak emission wavelengths of the scintillators (Table 1). The LEDs were powered using a current regulator assembled from a LM317 voltage regulator and standard circuit components. Output current was adjusted between 1 and 31 mA using a potentiometer. Power was provided by a 9-V battery. A schematic of the circuit can be found in Fig. 20.

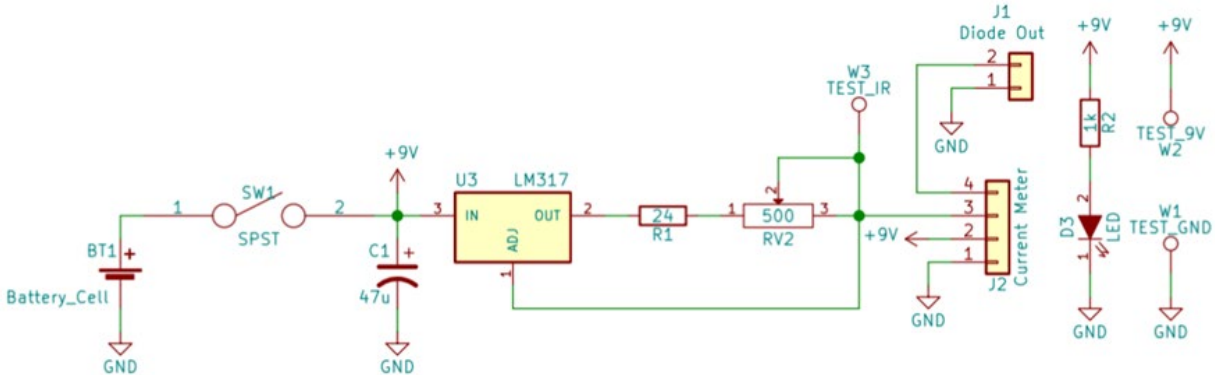


Fig. 20 LED current regulator circuit. The circuit consists of a 9-V battery, a linear voltage regulator, and a 500-ohm potentiometer, which regulates current from 1 to 31 mA

A 3D-printed enclosure was fabricated to enclose the LEDs and device under test to eliminate background light from calibration measurements. This enclosure featured multiple shelves housing neutral density (ND) filters used to attenuate the optical power emitted by the LEDs, as shown in Fig. 21. A calibrated silicon-based

optical power meter (Newport 818-UV) was used to measure the optical power output of the LEDs. Semiconductor power output during calibration was recorded using a Raspberry Pi controlled IV curve tracer, described in Section 3.4.

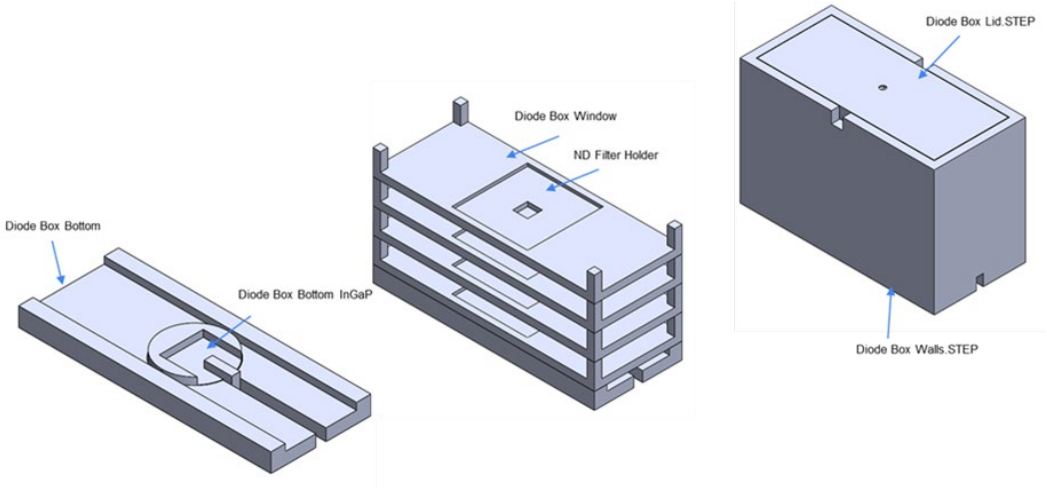


Fig. 21 Dark box test assembly consisting of a dual base for InGap and Emcore cells, a filter amount that 4 ND filters, and a changeable lid that fits multiple LEDs

The calibration data shown in Figs. 22 and 23 were used to assess the optical power generated from the scintillators. A fit was made to the three calibrations for the InGaP device measurements (Fig. 23) and is given by Eq. 6.

$$P_{electron} = 0.3148 \times P_{opt} + 0.042 \quad (6)$$

This relationship expresses electrical power output of the PV system as a function of optical power (P_opt) directed into the PV. It was used to decouple the incident alpha particle power, the scintillator optical power, and the PV electrical power. The Emcore calibration differs from the InGaP calibration in two ways. First, the InGaP is wavelength insensitive in the region evaluated (400–600 nm), while the Emcore is not. Second, the threshold for sensitivity (>10 μW) is larger for Emcore than that of InGaP (~1 μW). We characterize the sensitivity threshold as the region where electrical output varies, becoming unstable with reduced light intensity. This stability as a function of growing incident light intensity is apparent above 10-μW incident power. This compares to the optical intensity level of <1 μW for the InGaP electrical output stability with little variation.

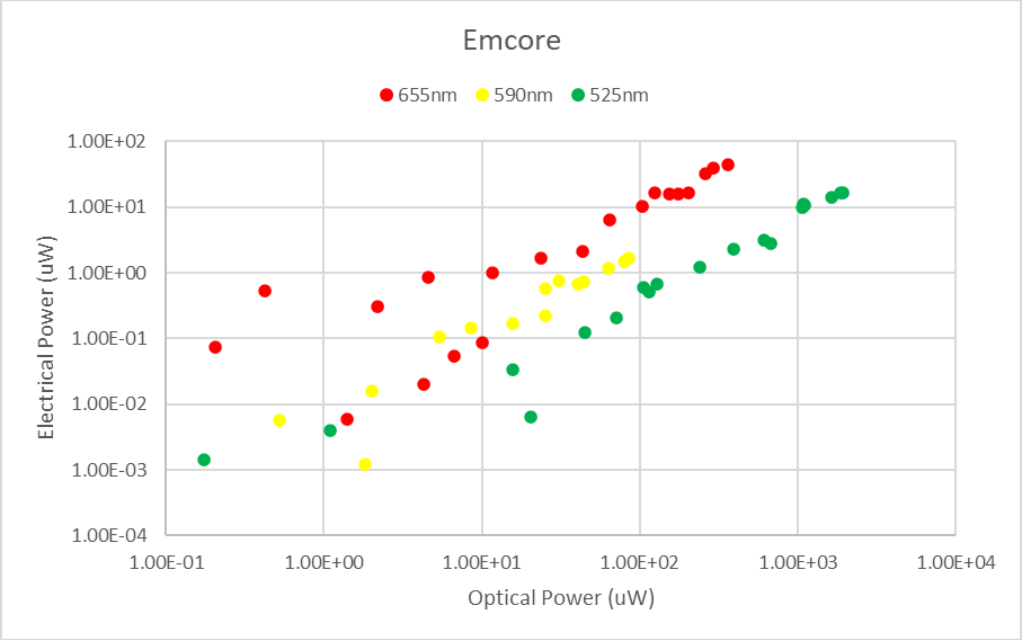


Fig. 22 Emcore calibration data using LED diodes with peak wavelength of 655 nm (red), 590 nm (yellow), and 525 nm (green). Optical power from 1 µW to 1.8 mW generates electrical power in the PV from 4 nW to 16 µW.

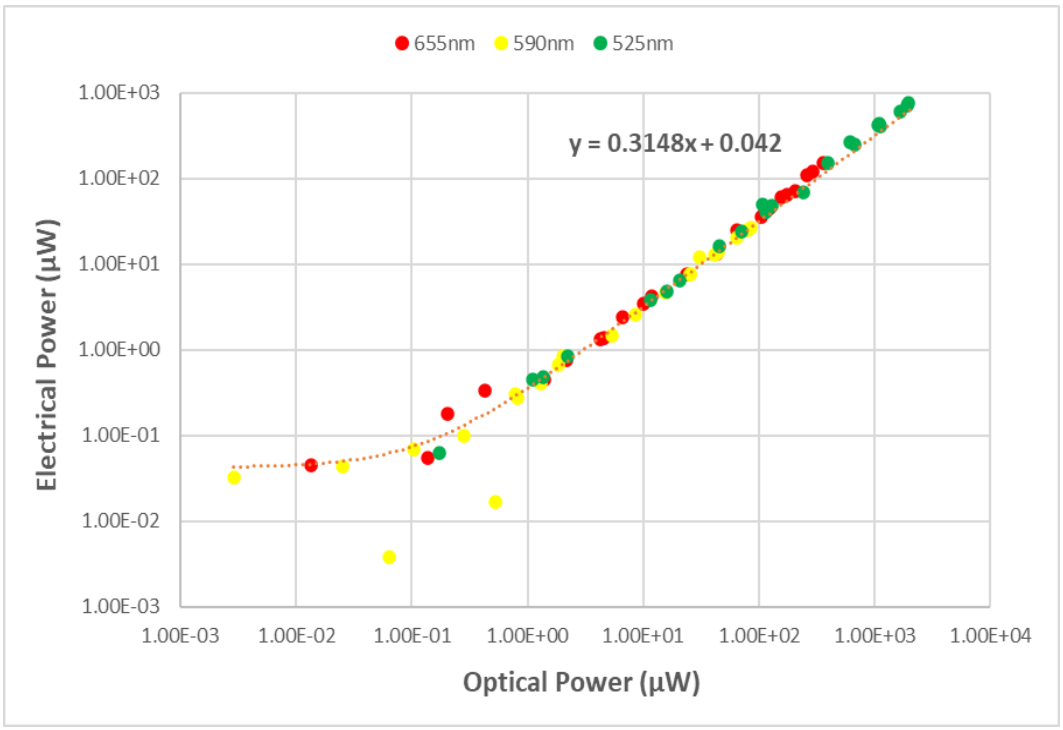


Fig. 23 InGaP calibration data obtained with 655 nm (red), 590 nm (yellow), and 525 nm (green) LEDs. Optical power from 10 nW to 1 mW generates electrical power in the PV from 50 nW to 900 µW.

4. Results

We measured the net system efficiency of scintillators on both a MicroLink InGaP PV and an Emcore triple-junction (TJ) PV cell. The net system efficiency is reported in Section 4.1 where the InGaP system power efficiency exceeds the TJ system power efficiency (see Eq. 5). The degradation of the selected scintillator luminosity is then compared among the scintillators in Section 4.2. All the scintillators were applied to glass slides before being mounted on the PV energy converters, protecting them from direct exposure. Section 4.3 discusses the absolute light yield of the scintillators. The results obtained using binders (2.5% by weight) mixed with the scintillating (polycrystalline) are provided in Section 4.4.

4.1 System Efficiency

System efficiencies for each scintillator, defined as the ratio of electrical power in the PV to the input alpha-beam power delivered by the pelletron, are provided in Figs. 24 and 25. Results from the Emcore PVs are not as precise as that of the InGaP PVs because the minimum threshold sensitivity of the InGaP is an order of magnitude greater than that of the TJ. The TJ was used to provide a coarse evaluation of the scintillator light yield in order to determine which scintillators should be investigated further on InGaP. System efficiency can be divided into PV efficiency and scintillator efficiency. The PV efficiency is a function of both wavelength and incident power level. Because of the difference in minimum detection threshold (~10 uW for Emcore and 1 uW for InGaP) efficiency values for scintillators evaluated on Emcore have larger error bars than their InGaP counterparts.

The scintillators investigated on InGaP PVs included CsI:Tl, Y_2O_2S:Eu, YAG:Eu, GdO_2S:Pr, and Y_2O_2S:Tb,Eu. System efficiency data is shown in Table 3 for both InGaP and Emcore PVs.

The system efficiency of CsI mounted on Emcore and InGaP PV is shown in Figs. 24 and 25. The measured system efficiency at a fluence of 10^{11} ions is 0.2% for InGaP as compared to 0.1% for CsI on Emcore. Efficiency values for the measured scintillators is shown in Table 3. The Emcore PV was half as efficient as the InGaP PV, making InGaP the superior choice for APV development.

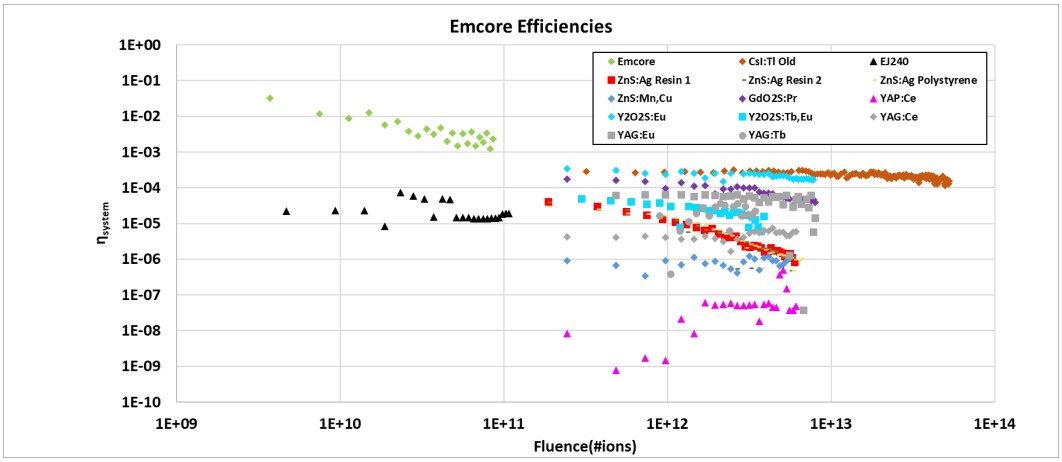


Fig. 24 System efficiency as a function of total ion fluence increases for various scintillators on Emcore PV

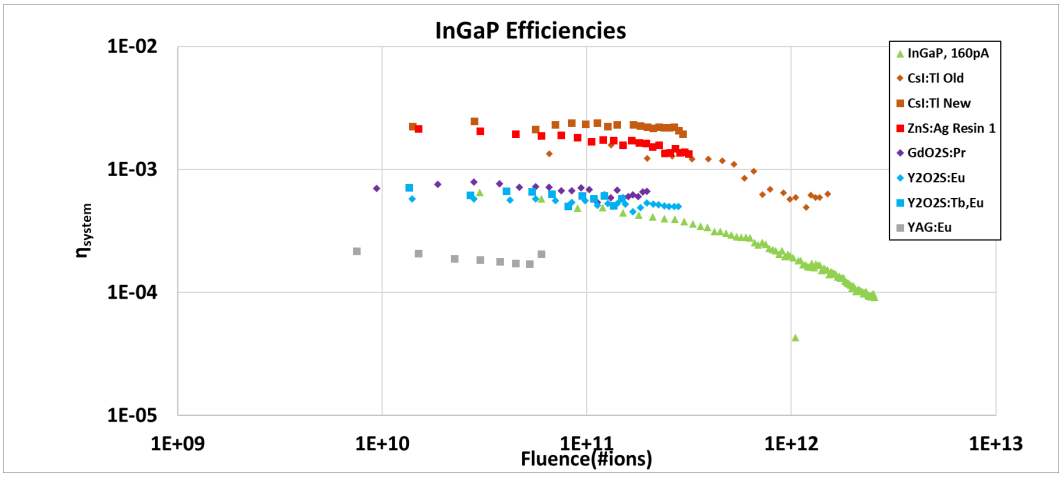


Fig. 25 System efficiency as a function of total ion fluence increases for various scintillators on InGaP PV

Table 3 System power efficiencies on PVs by scintillator

Scintillator	MPP(μW) (Emcore)	η_{system} on Emcore	MPP(μW) (InGaP)	η_{system} on InGaP
CsI:Tl	0.145	0.0716%	0.710	0.2244%
ZnS:Ag	0.169	0.0040%	0.641	0.1109%
GdO_2S:Pr	0.960	0.0175%	0.147	0.0697%
Y_2O_2S:Tb,Eu	0.162	0.0048%	0.216	0.0719%
Y_2O_2S:Eu	1.86	0.0340%	0.182	0.0575%
YAG:Eu	0.337	0.0061%	0.037	0.0217%

The maximum power point of each IV trace is shown in Figs. 26 and 27.

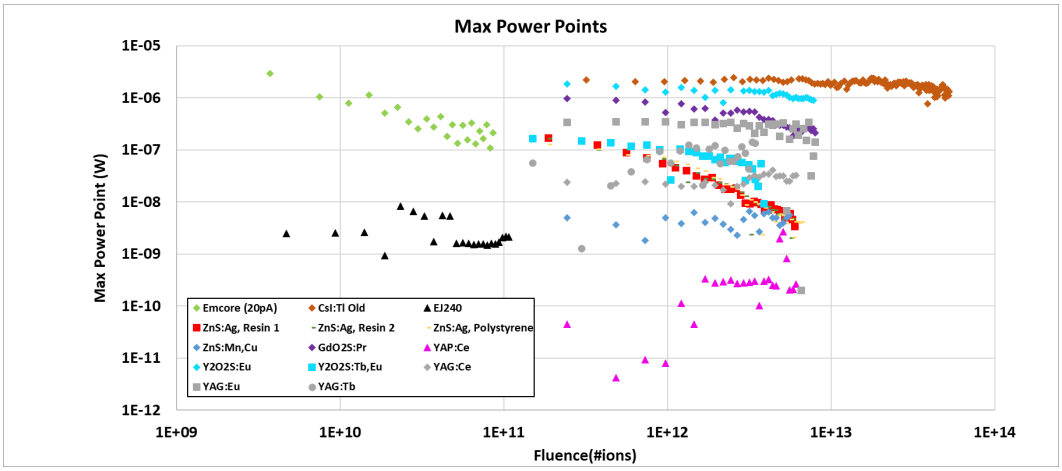


Fig. 26 Maximum power point measured on the Emcore PV as a function of total ion fluence, showing the initial value of luminosity as measured by the MPP of the IV curve trace. The degradation of the light yield with increasing ion flux is observed.

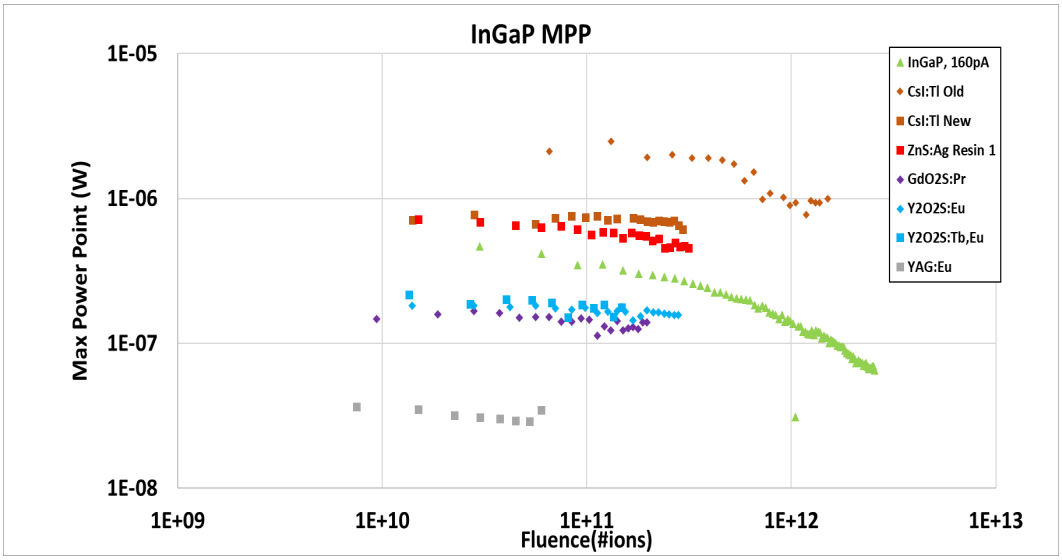


Fig. 27 Maximum power point measured by InGaP PV as a function of total ion fluence, showing the initial value of luminosity as measured by the MPP of the IV curve trace. The degradation of the light yield with increasing ion flux is observed.

The CsI:Tl scintillator coupled with the InGaP PV has the largest energy conversion efficiency (0.22%) of the materials evaluated, as shown in Table 3. The InGaP PV is three times more efficient than the Emcore at these power levels. However, the ratio between InGaP and Emcore is wavelength dependent in the 350- to 650-nm range.

4.2 Radiation Hardness

The radiation hardness of each scintillator was determined by evaluating the degradation of the system efficiency and MPP with radiation exposure. An operational lifetime for each scintillator can be determined by the ion fluence required to reduce the scintillator efficiency to 10% of the system's initial value. Scintillator performance degradation follows Eq. 7 (Birks and Black 1951; Hollerman et al. 1991, 2003), where a is proportional to half-power fluence level, n is ion fluence, and p is a fitting parameter. Using this equation, we can extrapolate scintillator performance beyond the range of the data that we have collected.

The CsI:Tl system's efficiency is shown in Fig. 28. Extrapolating from the data, approximately 3.51×10^{14} ions are needed to reduce the efficiency to 10% of its initial value. The lifetime exposure for ZnS:Ag was measured to be 2.63×10^{12} ions. Both data sets were collected on Emcore PV and demonstrate an improvement of 2 orders of magnitude in radiation hardness under alpha radiation exposure from ZnS:Ag to CsI:Tl.

$$\eta_{system} = 1 / (1 + [aN\text{^}p]) \tag{7}$$

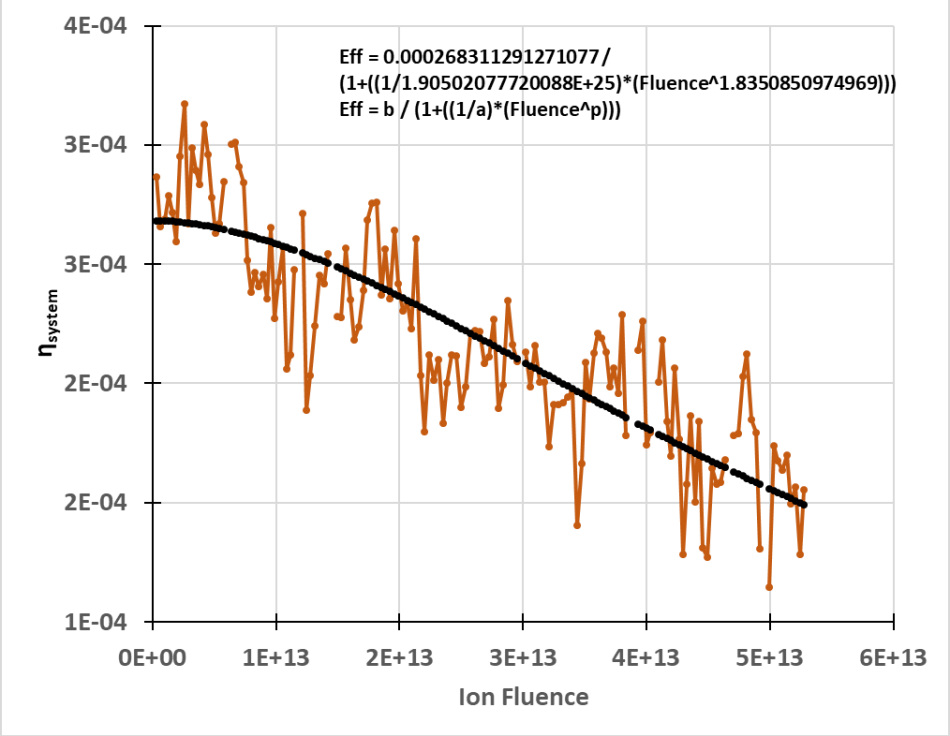


Fig. 28 Efficiency degradation during alpha-exposure of CsI:Tl on Emcore PV at I_{PELL} ~1.84 nA

4.3 Scintillator Luminosity

The MPP from the PV was measured using the pelletron. The peak luminosity of the scintillators was calculated from the pelletron parameters, the MPP, and calibration data using Eq. 8.

$$\eta_{scintillator} = \frac{MPP}{P_{pelletron}} \times \eta_{pv} \tag{8}$$

Here, $\eta_{scintillator}$ is the scintillator efficiency, $P_{pelletron}$ is the pelletron power, and η_{pv} is the PV efficiency given by Eq. 9.

$$\eta_{pv} = \frac{MPP}{P_{opt}} \tag{9}$$

where P_{opt} is the optical power originating from the scintillator. The value is obtained through Eq. 6.

The electrical power output from the PV can be obtained from Eqs. 8 and 9 using Eq. 10:

$$P_{pv} = P_{pelletron} \times \eta_{scintillator} \times \eta_{pv} \tag{10}$$

$$P_{ion} = I_{pelletron} \times \frac{\#\alpha}{q} \times E_{\alpha} \tag{11}$$

The pelletron ion beam power (P_{ion}) is given by Eq. 11. Here, $I_{pelletron}$ is the pelletron current, E_{α} is the energy of the alpha particles, and q is the ion charge.

$$\frac{\#ph}{MeV} = \frac{\frac{P_{pv}}{h\nu}}{P_{ion}} \tag{12}$$

Utilizing values from Eqs. 8–11, Eq. 12 outlines the calculation methodology for peak luminosity of the scintillators.

The wavelength of each scintillator and corresponding PV efficiency and phosphor efficiency are shown in Table 4. The MPP electrical output was measured, and the luminescence in units of photons/MeV was calculated through Eqs. 8–12. CsI:Tl possessed the largest luminosity of all scintillators.

Table 4 The measured PV efficiency, scintillator efficiency MPP, and emission photons from selected scintillators evaluated in this report

Scintillator	λ_{max} emission (nm)	Luminescence (kPh/MeV)	MPP (µW)	η_pv (%)	η_phos (%)
CsI:Tl	550	62.3	0.710	39	0.58
ZnS:Ag	450	57.4	0.641	39	0.65
Y_2O_2S:Tb,Eu	560	19.2	0.216	39	0.18
Y_2O_2S:Eu	615	16.9	0.182	39	0.15
Gd_2O_2S:Pr	510	16.7	0.147	39	0.18
ZnS:Cu,Al	525	9.8	0.257	39	0.09
YAG:Eu	580	4.2	0.037	39	0.06

4.4 Powder Scintillator Binder Comparison

To investigate the impact (luminosity) of the different binders used (supporting structure to mix with the polycrystalline scintillating powder formats), a comparison was made by acquiring ZnS:Ag data for each binder. The polystyrene binder (PS) yielded 40% higher system efficiency than UV resins as shown in Fig. 29. More data is required before the binders' effect on radiation hardness can be evaluated.

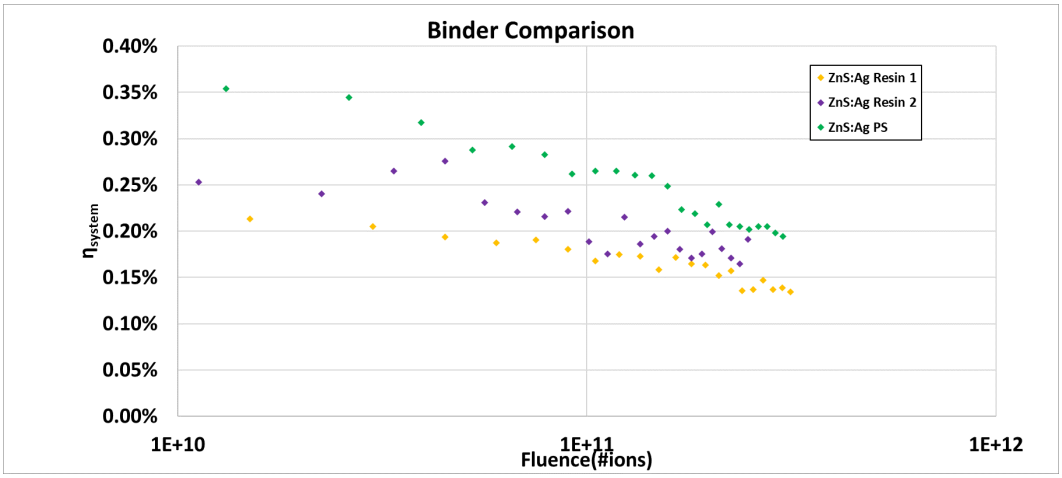


Fig. 29 Comparison of ZnS in three binders, all 2.5% by weight. The polystyrene light yield is 40% more luminous than Resin 1.

5. Conclusions and Future Work

The calculated alpha-induced luminosity for scintillating materials is given in Table 5. It was anticipated that alpha particles would yield a lower luminescent efficiency (ph/MeV) than electrons. This hypothesis was based on the data presented by Saint-Gobain (2021). The measured values for alpha-induced luminosity are compared to vendor-provided luminosity for electron-induced results.

Table 5 Comparison between electron- and alpha-induced photons

Scintillator	Electron induced (kPh/MeV)	Alpha induced (kPh/MeV)
CsI:Tl	54	62.3
ZnS:Ag	52.2	57.4
Y_2O_2S:Eu	25	16.9
Gd_2O_2S:Pr	9	16.7
YAG:Eu	25	4.2

Additional work and research must be undertaken to establish the validity of the data presented in Table 5 and to facilitate a meaningful comparison between the two data sets.

All the measurements presented in this report represent preliminary findings. The calibration measurements herein were taken using the LED diode box (Fig. 21). Additional spectral resolution when calibrating the scintillators is required for future experiments. This can be achieved using a larger range of LED sourced wavelengths if the correct LEDs can be found. Currently, we are developing a white light source that will be filtered through several notch (25 nm) and ND filters to produce the required calibration signal.

The peak emission wavelengths of all examined scintillators have been derived from both literature references and vendor listings. We intend to experimentally verify these values by performing spectral analysis on the scintillators.

We intend to explore novel scintillators that have been proposed (Derenzo et al. 2019; Dorenbos 2000) and examine machine learning approaches to find new scintillating compounds (Derenzo et al. 2003; Pilania et al. 2018) by optimizing luminosity and minimizing degradation of materials for APV systems. Through the technique of conducting experiments at higher ion beam fluences, we will perform accelerated testing of scintillation materials.

6. References

Bailey SG, Wilt DM, Castro SL, Cress CD, Raffaelle RP. Photovoltaic development for alpha voltaic batteries. Conference Record of the Thirty-first IEEE Photovoltaic Specialists Conference; 2005 Jan. IEEE. p. 106–109.

Berman VM, Litz M, Russo J. Investigation of electrical power degradation in beta photovoltaic (βPV) and beta voltaic (βV) power sources using 63Ni and 147Pm. 2018.

Birks JB, Black FA. Deterioration of anthracene under alpha-particle irradiation. Proc Phys Soc A. 1951;64(5):511.

Bizarri G. Scintillation mechanisms of inorganic materials: from crystal characteristics to scintillation properties. J Crystal Growth. 2010;312(8):1213–1215. doi:10.1016/j.jcrysgro.2009.12.063.

Cao W, Xue J. Recent progress in organic photovoltaics: device architecture and optical design. Energy Environ Sci. 2014;7(7):2123–2144.

Chase EW, Hepplewhite RT, Krupka DC, Kahng D. Electroluminescence of ZnS lumocen devices containing rare-earth and transition-metal fluorides. J Appl Phys. 1969;40(6):2512–2519.

Colerico CW, Serreze HB, Messenger SR, Burke EA, Xapsos MA. Alpha particle simulation of space radiation damage effects in semiconductor devices. IEEE Transactions on Nuclear Science. 1995;42(6):2089–2094. doi:10.1109/23.489257.

Cress CD, Landi BJ, Raffaelle RP, Wilt DM. InGaP alpha voltaic batteries: synthesis, modeling, and radiation tolerance. J Appl Phys. 2006;100(11).

Cress CD, Redino CS, Landi BJ, Raffaelle RP. Alpha-particle-induced luminescence of rare-earth-doped Y2O3 nanophosphors. J Solid State Chem. 2008;181(8):2041–2045.

Dai Y, Kum H, Slocum MA, Nelson GT, SM Hubbard. High efficiency single-junction InGaP photovoltaic devices under low intensity light illumination. 2017 IEEE 44th Photovoltaic Specialist Conference (PVSC); 2017; Washington, DC. p. 222–225. doi:10.1109/PVSC.2017.8366547.

Derenzo S, Boswell M, Weber M, Brennan K. Scintillator properties. Lawrence Berkeley National Laboratory (US); 2019. https://scintillator.lbl.gov.

Derenzo SE, Weber MJ, Bourret-Courchesne E, Klintenberg MK. The quest for the ideal inorganic scintillator. Nucl Instrum Meth Phys Res A. 2003;505(1–2):111–117.

Dorenbos P. The 5d level positions of the trivalent lanthanides in inorganic compounds. J Luminescence. 2000;91(3–4):155–176.

Gektin A, Korzhik M. Inorganic scintillators for detector systems. Springer; 2017. p. 20–77.

Guthoff M, de Boer W, Müller S. Simulation of beam induced lattice defects of diamond detectors using FLUKA. Nucl Instrum Meth Phys Res A. 2014;735: 223–228.

Holland LR, Jenkins GM, Fisher JH, Hollerman WA, Shelby GA. Efficiency and radiation hardness of phosphors in a proton beam. Nucl Instrum Methods Phys Res B. 1991;56–57:1239–1241. doi:10.1016/0168-583x(91)95141-y.

Hollerman WA, Fisher JH, Shelby GA, Holland LR, Jenkins GM. Proton damage measurements of rare earth oxide scintillators. IEEE Trans Nucl Sci. 1991;38(2):184–187. doi:10.1109/23.289294.

Hollerman WA, Allison SW, Goedeke SM, Boudreaux P, Guidry R, Gates E. Comparison of fluorescence properties for single crystal and polycrystalline YAG: Ce. 2002 IEEE Nuclear Science Symposium Conference Record. IEEE; 2003 Nov. p. 460–463.

Hong L, Tang XB, Xu ZH, Liu YP, Chen D. Parameter optimization and experiment verification for a beta radioluminescence nuclear battery. J Radioanal Nucl Chem. 2014;302:701–707.

Kumar V, Luo Z. A review on X-ray excited emission decay dynamics in inorganic scintillator materials. Photonics. 2021;8(3):71. doi:10.3390/photonics8030071.

Lecoq P. Inorganic scintillators for detector systems: physical principles and crystal engineering. Springer; 2007.

Nordlund K. Historical review of computer simulation of radiation effects in materials. J Nucl Mater. 2019;520:273–295.

Pfann WG, Van Roosbroeck W. Radioactive and photoelectric p-n junction power sources. J Appl Phys. 1954;25(11):1422–1434.

Pilania G, McClellan KJ, Stanek CR, Uberuaga BP. Physics-informed machine learning for inorganic scintillator discovery. J Chem Phys. 2018 June 28;148(24):241729. doi:10.1063/1.5025819.

Russo J, Litz M, Ray W, Smith B, Moyers R. A radioluminescent nuclear battery using volumetric configuration: 63Ni solution/zns:Cu,al/ingap. Appl Radiat Isot. 2017;130:66–74. doi:10.1016/j.apradiso.2017.09.018.

Rybicki G, Vargas-Aburto C, Uribe R. Silicon carbide alphavoltaic battery. In Conference Record of the Twenty Fifth IEEE Photovoltaic Specialists Conference; 1996 May. IEEE. p. 93–96.

Saint-Gobain. Organic scintillation materials and assemblies. Saint-Gobain; 2021 [accessed 2023 Sep 6]. https://luxiumsolutions.com/sites/default/files/2021-12/Organics-Plastic-Scintillators.pdf

Stan M, Sharps P, Fatemi N, Spadafora F, Aiken D, Hou H. Design and production of extremely radiation-hard 26% InGaP/GaAs/Ge triple-junction solar cells. Conference Record of the IEEE Photovoltaic Specialists Conference; 2000. p. 1374–1377. doi:10.1109/PVSC.2000.916148.

Stoller RE, Toloczko MB, Was GS, Certain AG, Dwaraknath S, Garner FA. On the use of SRIM for computing radiation damage exposure. Nucl Instrum Meth Phys Res B. 2013;310:75–80.

Tyagi M, Singh A, Banerjee D, Sugilal G, Kaushik CP. Radiation-resistant beta-photovoltaic battery using Ce-doped Gd3Ga3Al2O12 single-crystal scintillator. Appl Phys Lett. 2021;118(17).

Tzani MA, Gioftsidou DK, Kallitsakis MG, Pliatsios NV, Kalogiouri NP, Angaridis PA, Lykakis IN, Terzidis MA. Direct and indirect chemiluminescence: reactions, mechanisms and challenges. Molecules. 2021;26(24):7664.

Weber MJ. Inorganic scintillators: today and tomorrow. J Luminescence. 2002;100(1–4):35–45. doi:10.1016/s0022-2313(02)00423-4.

Werner CJ, et al. MCNP6.2 release notes. Los Alamos National Laboratory (US); 2018. Report No.: LA-UR-18-20808. doi:10.2172/1419730.

Wu J, Walukiewicz W, Yu KM, Shan W, Ager JW 3rd, Haller EE, Lu Hai, Schaff William J, Metzger WK, Kurtz S. Superior radiation resistance of In1ÀxGaxN alloys: full-solar-spectrum photovoltaic material system. J Appl Phys. 2003; 94(10):6477–6482. doi:10.1063/1.1618353.

Xu J, Guo M, Lu M, He H, Yang G, Xu J. Effect of alpha-particle irradiation on InGaP/GaAs/Ge triple-junction solar cells. Materials. 2018;11(6):944.

Xue S, Tan C, Kandlakunta P, Oksuz I, Hlinka V, Cao LR. Methods for improving the power conversion efficiency of nuclear-voltaic batteries. Nucl Instrum Methods Phys Res A. 2019;927:133–139.

Yamaguchi M, Khan A, Taylor SJ, Imaizumi M, Hisamatsu T, Matsuda S. A detailed model to improve the radiation-resistance of Si space solar cells. IEEE Trans Electron Dev. 1999;46(10):2133–2138. doi:10.1109/16.792008.

Yen W, Shionoya S, Yamamoto H. Phosphor Handbook. CRC Press; 2006.

Yost DC, Yao Y, Kanai Y. First-principles modeling of electronic stopping in complex matter under ion irradiation. J Phys Chem Lett. 2019;11(1):229–237.

Ziegler JF, Ziegler MD, Biersack JP. SRIM - the stopping and range of ions. Matter Nucl Instrum Methods Phys Res B. 2010;268(11–12):1818–1823. doi:10.1016/j.nimb.2010.02.091.

Zorn C. Studies in the radiation resistance of plastic scintillators: review and prospects. IEEE Trans Nucl Sci. 1990;37(2):504–512.

Zych E, Brecher C, Glodo J. Kinetics of cerium emission in a YAG:Ce single crystal: the role of traps. J Phys: Condens Matter. 2000;12:1947.

Appendix A. Scintillator Ranking

Maximizing energy conversion efficiency of a-particle kinetic energy to photons in a scintillator is important for creating a power-dense radio-photovoltaic power source. The search for highly luminous scintillating materials began with literature reviews in nuclear physics and particle accelerator journals, where the use of scintillating materials with high luminosity (sensitivity) and quickly decaying fluorescence (return to baseline for next particle appearance) help to detect alpha, beta, gamma, and neutron radiation. In addition, medical journals were used to understand how scintillators enable detection of radiation in medical diagnostics (positron emission tomography, nuclear magnetic resonance). Gamma and beta detection are essential in imaging and tomography for diagnosis. Luminosity and fast response are highly regarded qualities in scintillators for these applications. For radioisotope power generation, the highest-regarded qualities are luminosity and low degradation when subjected to high fluences of ions. Luminosity and material degradation characteristics for scintillators exposed to alpha particles are less of interest to commercial communities and therefore difficult to find in the literature. We collected information on the most luminous, most available, non-hygroscopic scintillating materials. The information collected is based on the figures of merit defined in Section 1 of this report.

The figure of merit analysis generates a ranking of the selected scintillators providing the greatest values for each material property. The top 10 rank of scintillators based on conversion efficiency is found in Table A-1 and radiation hardness in Tables A-2 through A-5.

Table A-1 Top high-output scintillators

Rank	Scintillator	Output (photons/MeV electron)
1	LuI_3:Ce	115
2	SrI_2:Eu	115
3	YI_3:Ce	99
4	$CsBa_2$:Eu	97
5	KSr_2I_5:Eu	94
6	KBa_2I_5:Eu	90
7	LSO ($LiCa_2I_5$:Eu)	90
8	GdI_3:Ce	89
9	CaI_2	86
10	CaI_2:Eu	86

Table A-2 Top high-density scintillators

Rank	Scintillator	Density (g/cc)
1	$CdWO_4$	7.9
2	Gd_2O_3	7.41
3	LSO (Lu_2SiO_5:Ce)	7.4
4	Gd_2O_2S:Pr	7.32
5	Gd_2O_2S	7.32
6	BGO ($Bi_4Ge_3O_{12}$)	7.13
7	LYSO ($Lu_2Y_2SiO_5$)	7.1
8	LAG ($Lu_3Al_5O_{12}$:Ce	6.73
9	GSO (Gd_2SiO_5)	6.71
10	GAGG ($Gd_3Al_2Ga_3O_{12}$:Ce)	6.63

Table A-3 Top high-melting-point scintillators

Rank	Scintillator	MP (°C)
1	Gd_2O_3	2420
2	Y_2O_2S:Eu	2350
3	Y_2O_2S	2350
4	GAGG ($Gd_3Al_2Ga_3O_{12}$:Ce)	2105
5	LSO (Lu_2SiO_5:Ce)	2100
6	LYSO ($Lu_2Y_2SiO_5$)	2050
7	LUAG ($Lu_3Al_5O_{12}$:Ce)	2020
8	P-47 (Y_2SiO_5:Ce)	2000
9	YAG ($Y_3Al_5O_{12}$:Ce)	1970
10	YAG:Eu	1970

Table A-4 Top high molar mass scintillators

Rank	Scintillator	Molar mass (AMU)
1	BGO ($Bi_4Ge_3O_{12}$)	100.00
2	$CsBa_2I_5$:Eu	83.66
3	KBa_2I_5:Eu	76.13
4	GAGG ($Gd_3Al_2Ga_3O_{12}$:Ce)	74.41
5	LUAG ($Lu_3Al_5O_{12}$:Ce)	68.38
6	KSr_2I_5:Eu	68.14
7	LCI ($LiCa_2I_5$:Eu)	57.93
8	$LuGdI_3$:Ce	57.23
9	LYSO ($Lu_2Y_2SiO_5$)	51.04
10	YAG ($Y_3Al_5O_{12}$:Ce)	47.65

Table A-5 Least vacancy prone scintillators

Rank	Scintillator	Least vacancy prone (vacancies)
1	stilbene (C_4H_{12})	182.1
2	ZnSe:O	178.8
3	BGO ($Bi_4Ge_3O_{12}$)	170.3
4	CaI_2:Eu	166.3
5	Mg,ZnF_2:Gd	164.8
6	LSO (Lu_2SiO_5:Ce)	163.7
7	LYSO ($Lu_2Y_2SiO_5$)	163.6
8	ZnS:Cu	159.7
9	ZnS:Si	159.7
10	ZnS:Ag	159.7

A complete list of the 66 scintillators evaluated is shown in Table A-6. Shown are the characteristics of scintillators and values for 1) luminous intensity under gamma stimulation, 2) density, 3) melting point, 4) atomic mass, and 5) vacancies created per alpha ion incident on the scintillator. These values contribute to the evaluation of figure of merit (FOM) for these scintillating materials. A graph of the ranked scintillating materials using FOM follows in Fig. A-1.

Table A-6 Characteristics of scintillators that form FOM

Scintillator	Chemical Formula	λ [nm]	intensity [ky/MeV e-]	density [g/cc]	melting point C	Mass [amu]	Vacancies per Ion	FOM
Anthracene	C14H10	350	17.40	1.25	216	178	123.9	6758
BC400B	[CH2CH(C6H4CH3)]n	423	11.31	1.03	175	118	140.5	1715
BC404	[CH2CH(C6H4CH3)]n	408	11.83	1.03	175	118	140.5	1794
BC408	[CH2CH(C6H4CH3)]n	425	11.14	1.03	175	118	140.5	1688
BC412	[CH2CH(C6H4CH3)]n	434	10.44	1.03	175	118	140.5	1583
BC420	[CH2CH(C6H4CH3)]n	391	11.14	1.03	175	118	140.5	1688
BC428	[CH2CH(C6H4CH3)]n	480	6.26	1.03	175	118	140.5	950
BC444	[CH2CH(C6H4CH3)]n	428	7.13	1.023	175	118	140.5	1074
BC521	[CH2CH(C6H4CH3)]n	424	10.44	1.03	175	118	140.5	1583
BGO	Bi4Ge3O12	480	10.00	7.13	1050	1246	170.3	547611
CaF2	CaF2	435	30.00	3.18	1360	78	149.1	67941
CaI2	CaI2	410	86.00	3.96	779	294	156.4	498514
CaI2:Eu	CaI2:Eu	470	86.00	3.96	779	294	166.3	468837
CdWO4	CdWO4	480	13.00	7.9	1871	360	154.3	448633
CsBa2I5:Eu	CsBa2:Eu	434	97.00	5	610	1042	140.2	2199014
CsI(Na)	CsI	420	41.00	4.51	894	260	134.9	318377
CsI(Tl)	CsI	550	54.00	4.51	894	260	134.9	419326
EJ204	[CH2CH(C6H4CH3)]n	408	10.40	1.023	175	118	140.5	1566
EJ228	[CH2CH(C6H4CH3)]n	391	10.20	1.023	175	118	140.5	1536
EJ240	[CH2CH(C6H4CH3)]n	430	6.30	1.023	175	118	140.5	949
EJ260	[CH2CH(C6H4CH3)]n	490	9.20	1.023	175	118	140.5	1385
EJ262	[CH2CH(C6H4CH3)]n	481	8.70	1.023	175	118	140.5	1310
EJ290	[CH2CH(C6H4CH3)]n	423	9.00	1.02	175	118	140.5	1351
EJ296	[CH2CH(C6H4CH3)]n	435	9.00	1.02	175	118	140.5	1351
EJ440	[CH2CH(C6H4CH3)]n	450	52.20	1.02	175	118	140.5	7837
EJ442	[CH2CH(C6H4CH3)]n	450	52.20	1.02	175	118	140.5	7837
EJ444	[CH2CH(C6H4CH3)]n	423	11.31	1.023	175	118	140.5	1703
EJ600	ZnS:Ag	450	52.20	2.5	1850	97	159.7	147304
GAGG	$Gd_3Al_2Ga_3O_{12}$:Ce	520	50.00	6.63	2105	927	144.6	4472849
Gd2O2S:Pr	Gd2O2S:Pr	510	9.00	7.32	1050	379	144.1	181724
Gd2O2S:Tb	Gd2O2S	515	9.00	7.32	1050	379	144.1	181724
Gd2O3	Gd2O3	515	2.10	7.41	2420	362	140.8	96952
GdI3:Ce	GdI3:Ce	563	89.00	5.2	925	538	150.8	1527167
GSO	Gd2SiO5	440	9.00	6.71	1900	423	152.4	318160
KBa2I5:Eu	KBa2I5:Eu	444	90.00	4.52	569	948	141.5	1551221
KCaI3:Eu	KCaI3:Eu	465	72.00	3.81	520	460	146.7	447184
KSr2I5:Eu	KSr2I5:Eu	445	94.00	4.39	470	849	148.4	1109412
LCI	LiCa2I5:Eu	472	90.00	3	610	722	153.3	775286
LSO	Lu2SiO5:Ce	256	25.00	7.4	2100	458	163.7	1086985
LUAG	Lu3Al5O12:Ce	510	15.00	6.73	2020	852	140.1	1239818
LuGd Halide	LuGdI3:Ce	540	78.00	5.4	925	713	147.0	1889557
LuI3:Ce	LuI3:Ce	540	115.00	5.6	1050	556	159.1	2361729
LYSO	$Lu_2Y_2SiO_5$	420	30.00	7.10	2050	636	163.6	1697032
MgF2:Gd	Mg,ZnF2	315	1.00	3.15	1263	62	123.7	2004
P47	Y2SiO5:Ce	400	3.80	4.40	2000	286	145.8	65571
PVT	[CH2CH(C6H4CH3)]n	425	11.14	1.03	175	118	140.5	1688
SrAl2O4:Dy	SrAl2O4	522	46.00	3.56	1200	206	125.2	322676
SrAl2O4:Eu	SrAl2O4	365	42.00	3.56	1200	206	125.2	294617
SrI2:Eu	SrI2:Eu	435	115.00	4.55	538	341	144.5	665157
SrI2:Eu	SrI2:Eu	435	115.00	4.55	538	341	144.5	665157
stilbene	C4H12	290	17.40	0.971	125	60	182.1	697
Y2O2S:Eu	Y2O2S:Eu	615	2.10	2.88	2350	242	135.3	25408
Y2O2S:Tb	Y2O2S	530	2.10	2.88	2350	242	135.3	25408
YAG:Ce	Y3Al5O12	560	15.00	4.56	1970	594	126.4	632823
YAG:Eu	YAG:Eu	580	15.00	4.56	1970	594	126.4	632823
YAG:Tb	YAG:Tb	560	15.00	4.56	1970	594	126.4	632823
YAP	YAlO3	370	25.00	5.37	1875	164	129.2	319296
YAP:Ce	Y3Al5O12	550	25.00	5.37	1875	164	129.2	319296
YAP:Eu	YAlO3	545	25.00	5.37	1875	164	129.2	319296
YAP:Tb	YAlO3	580	25.00	5.37	1875	164	129.2	319296
YI3:Ce	YI3:Ce	549	98.60	4.6	1004	470	147.1	1453790
Yttrium Silica	Y1Si2O7:Ce3+	378	11.68	2.054	400	257	150.2	16424
ZnF2:Gd	Mg,ZnF2	560	1.00	4.84	872	103	164.8	2647
ZnS:Cu	ZnS:Cu	550	52.20	4.09	1850	97	159.7	240989
ZnS:Si	ZnS	550	52.20	4.09	1850	97	159.7	240989
ZnSe:O	ZnSe:O	595	71.00	5.42	1100	144	178.8	341719

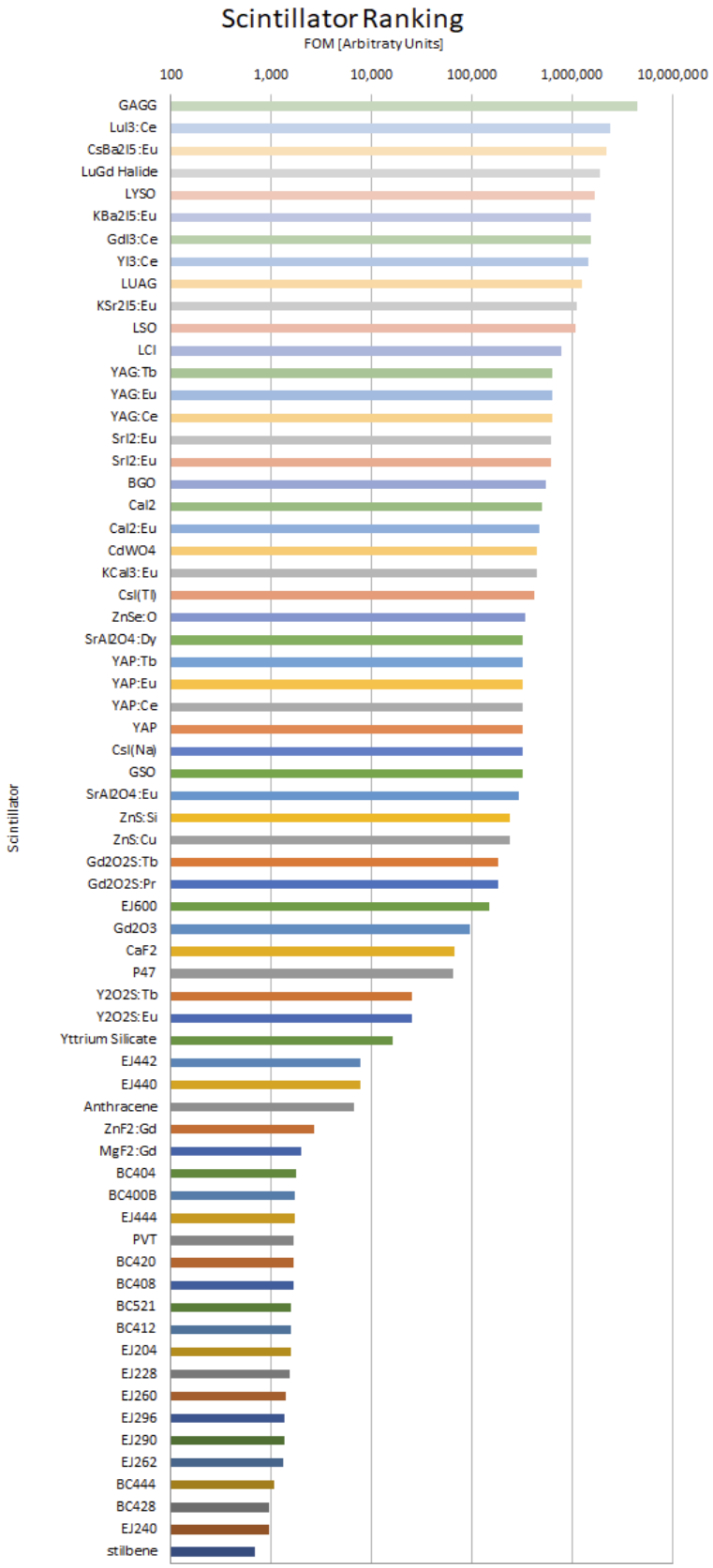


Fig. A-1 Ranked scintillating materials using FOM

Appendix A References

For Table A-7

Derenzo S, Boswell M, Weber M, Brennan K. Scintillator Properties. Berkeley Lab; 2019. https://scintillator.lbl.gov.

Anthracene

Haynes WM, editor. CRC Handbook of Chemistry and Physics. 92nd ed. CRC Press; 2011. ISBN 978-1439855119.

BaBr

Gundiah G, Bizarri G, Hanrahan SM, Weber MJ, Bourret-Courchesne ED, Derenzo SE. Structure and scintillation of Eu(2+)-activated solid solutions in the BaBr(2)-BaI(2) system. Nucl Instrum Meth Phys Res A. 2011;652:234–237.

BaBrIEu

Bizarri G, Bourret-Courchesne ED, Yan Z, Derenzo SE. Scintillation and optical properties of BaBrI:Eu2+ and CsBa2I5:Eu. IEEE Trans Nucl Sci. 2011;58:3403–3410.

BC400B

https://www.crystals.saint-gobain.com/radiation-detection-scintillators/plastic-scintillators/bc400-bc404-bc408-bc412-bc416#

https://seltokphotonics.com/upload/iblock/f5f/f5f21e0ae0abc57430fca2642873553a.pdf

BC404

https://www.crystals.saint-gobain.com/radiation-detection-scintillators/plastic-scintillators/bc400-bc404-bc408-bc412-bc416#

https://seltokphotonics.com/upload/iblock/f5f/f5f21e0ae0abc57430fca2642873553a.pdf

BC408

https://luxiumsolutions.com/radiation-detection-scintillators/plastic-scintillators/bc400-bc404-bc408-bc412-bc416

https://seltokphotonics.com/upload/iblock/f5f/f5f21e0ae0abc57430fca2642873553a.pdf

BC412

https://luxiumsolutions.com/radiation-detection-scintillators/plastic-scintillators/bc400-bc404-bc408-bc412-bc416

https://seltokphotonics.com/upload/iblock/f5f/f5f21e0ae0abc57430fca2642873553a.pdf

BC420

https://www.crystals.saint-gobain.com/sites/hps-mac3-cma-crystals/files/2021-09/BC418-420-422%20Data%20Sheet.pdf

https://seltokphotonics.com/upload/iblock/f5f/f5f21e0ae0abc57430fca2642873553a.pdf

BC428

https://www.crystals.saint-gobain.com/radiation-detection-scintillators/plastic-scintillators/green-emitting-bc-428#

https://seltokphotonics.com/upload/iblock/f5f/f5f21e0ae0abc57430fca2642873553a.pdf

BC444

https://www.crystals.saint-gobain.com/radiation-detection-scintillators/plastic-scintillators/long-timing-constant-bc-444#

https://seltokphotonics.com/upload/iblock/f5f/f5f21e0ae0abc57430fca2642873553a.pdf

BC521

https://seltokphotonics.com/upload/iblock/f5f/f5f21e0ae0abc57430fca2642873553a.pdf

BGO

https://www.crytur.cz/materials/bgo/

CaF2

https://www.advatech-uk.co.uk/caf2_eu.html

CaI2Eu

Hofstadter R, inventor; Harshaw/Filtrol Partnership A Partnership of Kewanee Oil Co, assignee. Europium activated strontium iodide scintillators. United States patent US 3,373,279. 1968.

https://www.douglas-scott-mcgregor.com/uploads/1/3/3/5/133545016/arms-2018.pdf

https://www.chemicalbook.com/ProductChemicalPropertiesCB0235608_EN.htm

CdWO4

https://www.meta-laser.com/scintillation-detector/cdwo4-scintillation-detector.html

CsBa2I5Eu

Bourret-Courchesne ED, Bizarri G, Borade R, Yan Z, Hanrahan SM, Gundiah G, Chaudhry A, Canning A, Derenzo SE. Eu2+ -doped Ba2CsI5, a new high-performance scintillator. Nucl Instrum Meth Phys Res A. 2009;612:138–142.

CsI(Na)

Advatech UK Limited. Scintillator properties. CSI(NA) - cesium iodide (na) scintillator crystal. Advatech UK Limited; n.d. [accessed 2023 Sep 6]. https://www.advatech-uk.co.uk/csi_na.html

CsI(Tl)

Saint Gobain. Crystals. Saint Gobain; n.d. [accessed 2023 Sep 6]. https://www.crystals.saint-gobain.com/radiation-detection-scintillators/crystal-scintillators/csi-cesium-iodide#

EJ204

https://eljentechnology.com/products/plastic-scintillators/ej-200-ej-204-ej-208-ej-212

EJ228

https://eljentechnology.com/products/plastic-scintillators/ej-228-ej-230

EJ240

https://eljentechnology.com/products/plastic-scintillators/ej-240

EJ260

https://eljentechnology.com/products/plastic-scintillators/ej-260-ej-262

EJ262

https://eljentechnology.com/products/plastic-scintillators/ej-260-ej-262

EJ290

https://eljentechnology.com/products/plastic-scintillators/ej-290

EJ296

https://eljentechnology.com/products/plastic-scintillators/ej-296

EJ440

https://eljentechnology.com/products/zinc-sulfide-coated/ej-440-ej-442

EJ442

https://eljentechnology.com/products/zinc-sulfide-coated/ej-440-ej-442

EJ444

https://eljentechnology.com/products/zinc-sulfide-coated/ej-444?highlight=WyJhbnRocmFjZW5lIl0=

EJ600 (ZnS:Ag)

https://eljentechnology.com/products/zinc-sulfide-coated/ej-600

GAGG

www.meta-laser.com/scintillation-detector

https://www.epic-crystal.com/oxide-scintillators/gagg-ce-scintillator.html

Gd2O2S:Pr

Nakamura R. Improvements in the X-ray Characteristics of Gd2O2S:Pr Ceramic Scintillators. J Am Ceram Soc. 2004;82:2407–2410. doi:10.1111/j.1151-2916.1999.tb02097.x.

Gd2O2S:Tb

Chen L, Wu Y, Huo H, Tang B, Ma X, Wang J, Sun C, Sun J, Zhou S.. Nanoscale Gd2O2S:Tb Scintillators for High-Resolution Fluorescent Imaging of Cold Neutrons. ACS Appl Nano Mater. 2022,5(6);8440–8447. doi:10.1021/acsanm.2c01561.

Gd2O3

https://www.sciencedirect.com/science/article/pii/S0925346719306883

GdI3Ce

Grippa AY, Datsko YN, Zelenskaya OV, Kosinov NN. Synthesis and scintillation properties of GdCl3:Ce3+ (Gd1-xCexCl3, x = 0.005-0.08). Radiat Meas. 2010;45:398–39.

GSO

Melcher CL, Schweitzer JS, Utsu T, Akiyama S**.** Scintillation properties of GSO. IEEE Trans Nucl Sci. 1990 Apr;37(2):161–164. doi:10.1109/23.106611.

KBa2I5Eu

Stand L, Zhuravleva M, Chakoumakos B, Johnson J, Lindsey A, Melcher CL. Scintillation properties of Eu2+ -doped KBa2I5 and K2BaI4. J Luminescence. 2016;169:301.

KCaI3Eu

Lindsey AC, Zhuravleva M, Stand L, Wu Y, Melcher CL. Crystal growth and characterization of europium doped KCaI3, a high light yield scintillator. Opt Mater. 2015;48:1.

https://www.researchgate.net/publication/309371876_Scintillators_Quaternary_Iodide_KCaSrI_3_Eu_2_Single-Crystal_Scintillators_for_Radiation_Detection_Crystal_Structure_Electronic_Structure_and_Optical_and_Scintillation_Properties_Advanced_Optical_Mate/figures?lo=1&utm_source=google&utm_medium=organic

KSr2I5Eu

Stand L, Zhuravleva M, Lindsey A, Melcher CL. Growth and characterization of potassium strontium iodide: A new high light yield scintillator with 2.4% energy resolution. Nucl Instrum Meth Phys Res A. 2015;780:40.

LaBr

Cherepy NJ, Payne SA, Asztalos SJ, Hull G, Kuntz JD, Niedermayr T, Pimputkar S, Roberts JJ, Sanner RD, Tillotson TM, et al. E. Scintillators with potential to supersede lanthanum bromide. IEEE Trans Nucl Sci. 2009;56:873–880.

LCI

Soundara-Pandian L, Hawrami R, Glodo J, Ariesanti E, van Loef EV, Shah K. Lithium alkaline halides—next generation of dual mode scintillators. IEEE Trans Nucl Sci. 2016 Apr;63(2): 490–496. doi:10.1109/TNS.2016.2535355.

LiCa2I5Eu

Soundara-Pandian L, Hawrami R, Glodo J, Ariesanti E, van Loef EV, Shah K. Lithium alkaline halides—next generation of dual mode scintillators. IEEE Trans Nucl Sci. 2016;63:490–496.

LSO

Pepin CM, Berard P, Perrot A-L, Pepin C, Houde D, Lecomte R, Melcher CL, Dautet H. Properties of LYSO and recent LSO scintillators for phoswich PET detectors. IEEE Trans Nucl Sci. 2004 June;51(3):789–795. doi:10.1109/TNS.2004.829781.

LUAG

www.meta-laser.com/scintillation-detector

https://www.advatech-uk.co.uk/luag_ce.html

LuGdl3Ce & GdI3Ce (Halide)

Glodo J, Van Loef EVD, Higgins WM, Shah KS. Mixed lutetium iodide compounds. IEEE Trans Nucl Sci. 2008;NS-55:1496–1500.

Shah KS, Higgins WM, Van Loef EV, Glodo J, inventors; Radiation Monitoring Devices Inc, assignee. Lutetium gadolinium halide scintillators. United States patent US 7755054B1. https://patents.google.com/patent/US7755054

LuI3Ce

Birowosuto MD, Dorenbos P, de Haas JTM, van Eijk CWE, Kramer KW, Gudel HU. Optical spectroscopy and luminescence quenching of LuI3 : Ce3+. J Luminescence. 2006;118:308–316.

https://www.chemicalbook.com/ProductChemicalPropertiesCB6471950_EN.htm

LYSO

https://www.meta-laser.com/scintillation-detector/

MgF2:Gd

https://www.icc.ltd/magnesium-fluoride-material/

https://www.sciencedirect.com/science/article/pii/S0025540817324947

P47

https://www.tedpella.com/Scintillators_html/Scintillators.aspx#P47

https://en.wikipedia.org/wiki/Phosphor

PVT

Alex L, Paulraj R, Sonu, Tyagi M. Development of large size fast timing and radiation resistant PVT-based plastic scintillator detector. J Mater Sci Mater Electron. 2023;34:127. https://doi.org/10.1007/s10854-022-09577-9

https://www.sigmaaldrich.com/US/en/product/aldrich/755680

https://chalcogen.ro/83_RoslanNNN.pdf https://core.ac.uk/reader/334782090

https://www.sciencedirect.com/science/article/am/pii/S0925346718303537

SrAl2O4:Dy

https://tohoku.elsevierpure.com/en/publications/photoluminescence-and-scintillation-properties-of-eu-doped-stront

https://www.mdpi.com/2079-4991/13/14/2034/pdf

https://www.sciencedirect.com/science/article/pii/S0925346718303537

SrAl2O4:Eu

https://tohoku.elsevierpure.com/en/publications/photoluminescence-and-scintillation-properties-of-eu-doped-stront https://www.mdpi.com/2079-4991/13/14/2034/pdf

https://www.sciencedirect.com/science/article/pii/S0925346718303537

SrI2Eu

Rowe E, Bhattacharya P, Tupitsyn E, Groza M, Burger A, Cherepy NJ, Payne SA, Sturm BW, Pedrini C. A new lanthanide activator for iodide based scintillators: Yb2+. IEEE Trans Nucl Sci. 2013;60:1057.

van Loef EV, Wilson CM, Cherepy NJ, Hull G, Payne SA, Choong W-S, Moses WW, Shah KS. Crystal growth and scintillation properties of strontium iodide scintillators. IEEE Trans Nucl Sci. 2009;56:869–872.

https://www.douglas-scott-mcgregor.com/uploads/1/3/3/5/133545016/arms-2018.pdf

Stilbene

Lee SK, Son JB, Jo KH, Kang BH, Kim GD, Seo H, Park SH, Galunov NZ, Kim YK. Development of large-area composite stilbene scintillator for fast neutron detection. J Nucl Sci Technol. 2014;51(1):37–47. doi:10.1080/00223131.2014.845539.

Y2O2S:Eu

Lee SK, Son JB, Jo KH, Kang BH, Kim GD, Seo H, Park SH, Galunov NZ, Kim YK. Development of large-area composite stilbene scintillator for fast neutron detection. J Nucl Sci Technol. 2014;51(1);37–47. doi:10.1080/00223131.2014.845539.

Y2O2S:Tb

https://digital.csic.es/bitstream/10261/134597/1/Ionoluminescent.pdf

YAG:Ce

www.meta-laser.com/scintillation-detector

https://www.tedpella.com/Scintillators_html/Scintillators.aspx

https://www.emsdiasum.com/scintillators-for-scanning-electron-microscopes

https://www.crytur.cz/materials/yagce/ http://www.epic-scintillator.com/YAG-scintillator-6x6x1mm https://www.advatech-uk.co.uk/yag_ce.html

YAG:Eu

Kurlov VN, Klassen NV, Dodonov AM, Shmurak SZ, Strukova GK, Shmyt'ko IM, Derenzo SE, Weber MJ. Growth of YAG:Re3+ (Re=Ce, Eu)-shaped crystals by the EFG/Stepanov technique. Nucl Instrum Meth Phys Res A. 2005;537(1–2):21. doi:10.1016/j.nima.2004.08.007.

YAG:Tb

Kang YC, Lenggoro IW, Park SB, Okuyama K. Photoluminescence characteristics of YAG:Tb phosphor particles with spherical morphology and non-aggregation. J Phys Chem Solids. 1999 Nov;60(11):1855–1858. doi:10.1016/S0022-3697(99)00191-2.

YAP

www.meta-laser.com/scintillation-detector

https://www.tedpella.com/Scintillators_html/Scintillators.aspx

https://www.emsdiasum.com/scintillators-for-scanning-electron-microscopes

YAP:Ce

Moszyński M, et al. Properties of the YAP: Ce scintillator. Nucl Instrum Meth Phys Res A. 1999 Nov;404.1(1998):157–165.

www.meta-laser.com/scintillation-detector

https://www.tedpella.com/Scintillators_html/Scintillators.aspx

https://www.emsdiasum.com/scintillators-for-scanning-electron-microscopes

YAP:Eu

www.meta-laser.com/scintillation-detector

https://www.tedpella.com/Scintillators_html/Scintillators.aspx

https://www.emsdiasum.com/scintillators-for-scanning-electron-microscopes

YAP:Tb

www.meta-laser.com/scintillation-detector

https://www.tedpella.com/Scintillators_html/Scintillators.aspx

https://www.emsdiasum.com/scintillators-for-scanning-electron-microscopes

YI3Ce

Cherginets VL, Ponomarenko TV, Trefilova LN, Rebrova NV, Kosinov NN, Alekseev VD, Zelenskaya OV. Preparation and scintillation properties of YCl3:Ce crystals. Inorg Mater. 2009;45:946–948.

Cherginets VL, Rebrova TP, Ponomarenko TV, Tarasenko OA, Kosinov NN, Zelenskaya OV. Scintillation properties of Ce3+-doped YCl3 and YBr3. Radiat Measure. 2012;47:917.

https://www.chemicalbook.com/ChemicalProductProperty_US_CB5188488.aspx

Yttrium Silicate

https://digital.csic.es/bitstream/10261/134597/1/Ionoluminescent.pdf

https://www.tedpella.com/Scintillators_html/Scintillators.aspx

ZnF2:Gd

https://ieeexplore.ieee.org/document/6180198

ZnS:Cu

http://www.hep.ph.ic.ac.uk/fets/pepperpot/docs+papers/zns_602.pdf

https://www.science.gov/topicpages/z/zns+scintillator+light

https://www.hindawi.com/journals/ijp/2017/6752984/

ZnS:Si

http://www.hep.ph.ic.ac.uk/fets/pepperpot/docs+papers/zns_602.pdf

https://www.science.gov/topicpages/z/zns+scintillator+light

ZnSe:O

Kim YK, Kim JK, Lee WG, Kim SY, Kim BI, Ha JH, Starzhinskiy N, Ryzhikov V, Grinyov B. Properties of semiconductor scintillator ZnSe: O. Nucl Instrum Meth Phys Res A. 2007;580:258–261.

https://www.chemicalbook.com/ProductChemicalPropertiesCB8853039_EN.htm

Appendix B. Monte Carlo N-Particle (MCNP) Input Cards

The following MCNP input deck is the source of all the MCNP results created and discussed in Section 2 of this report.

```
.00 ZnS InGaP hybrid
c
c +z axis alpha beam
c
c +-------------------------------------------------------+
c |                    Cell Cards                         |
c +-------------------------------------------------------+
c # mat   density   surface       data
c Pb
 1  1   -2.5    -1   imp:e,p,a  1 u=1   $ZnS barrier
 2  1   -2.5    -2   imp:e,p,a  1 u=1   $ZnS barrier
 3  1   -2.5    -3   imp:e,p,a  1 u=1   $ZnS barrier
 4  1   -2.5    -4  imp:e,p,a  1 u=1   $ZnS barrier
 5  1   -2.5    -5  imp:e,p,a  1 u=1   $ZnS barrier
 6  1   -2.5    -6  imp:e,p,a  1 u=1   $ZnS barrier
 7  1   -2.5    -7  imp:e,p,a  1 u=1   $ZnS barrier
 8  1   -2.5    -8  imp:e,p,a  1 u=1   $ZnS barrier
 9  1   -2.5    -9  imp:e,p,a  1 u=1   $ZnS barrier
 10  1   -2.5    -10  imp:e,p,a  1 u=1   $ZnS barrier
 11  1   -2.5    -11  imp:e,p,a  1 u=1   $ZnS barrier
 12  1   -2.5    -12  imp:e,p,a  1 u=1   $ZnS barrier
 13  1   -2.5    -13  imp:e,p,a  1 u=1   $ZnS barrier
 14  1   -2.5    -14  imp:e,p,a  1 u=1   $ZnS barrier
 15  1   -2.5    -15  imp:e,p,a  1 u=1   $ZnS barrier
 16  4   -4.6    -16  imp:e,p,a  1 u=1   $InGaP PV
 17  1   -2.5 -17 16 15 14 13 12 11 10 9 8 7 6 5 4 3 2 1 &
     imp:e,p,a 1  u=1 $ZnS
 18  5   -4.6    -18 17  imp:e,p,a  1 u=1 $InGaP Shield
c air encasing
 31  2  -0.00129  -31 18 imp:e,p,a 1  u=1
 32  0     31          imp:e,p,a 1  u=1
c room
 34  2    -0.00129   -32  imp:e,p,a 1 fill=1
 35  0               32  imp:e,p,a 0      $outside world

c +-------------------------------------------------------+
c |                   Surface Cards                       |
c +-------------------------------------------------------+
c # type params
c
 1   rpp  -.0015 .0015  -.0015 .0015  0    .0003 $ZnS barrier
 2   rpp  -.0015 .0015  -.0015 .0015  0.0003 .0006  $ZnS barrier
 3   rpp  -.0015 .0015  -.0015 .0015  0.0006 .0009  $ZnS barrier
 4   rpp  -.0015 .0015  -.0015 .0015  0.0009 .0012  $ZnS barrier
 5   rpp  -.0015 .0015  -.0015 .0015  0.0012 .0015  $ZnS barrier
 6   rpp  -.0015 .0015  -.0015 .0015  0.0015 .0018  $ZnS barrier
 7   rpp  -.0015 .0015  -.0015 .0015  0.0018 .0021  $ZnS barrier
 8   rpp  -.0015 .0015  -.0015 .0015  0.0021 .0024  $ZnS barrier
 9   rpp  -.0015 .0015  -.0015 .0015  0.0024 .0027  $ZnS barrier
 10   rpp  -.0015 .0015  -.0015 .0015  0.0027 .0030  $ZnS barrier
 11   rpp  -.0015 .0015  -.0015 .0015  0.0030 .0033  $ZnS barrier
```

```
 12   rpp  -.0015 .0015  -.0015 .0015  0.0033 .0036  $ZnS barrier
 13   rpp  -.0015 .0015  -.0015 .0015  0.0036 .0039  $ZnS barrier
 14   rpp  -.0015 .0015  -.0015 .0015  0.0039 .0042  $ZnS barrier
 15   rpp  -.0015 .0015  -.0015 .0015  0.0042 .0045  $ZnS barrier
 16   rpp  -.0015 .0015  -.0015 .0015 .0045 .0080  $InGaP PV
 17   rpp  -0.008 0.008    -0.008 0.008    -0.008 0.008 $air
 18   rpp  -0.03 0.03    -0.03 0.03    -0.03 0.03  $InGaP
c air background
31   rpp  -0.05 0.05    -0.05 0.05    -0.05 0.05
c room dimensions
32   rpp  -0.052 0.052  -0.052 0.052  -0.052 0.052

c +-------------------------------------------------------+
c |                   Material Cards                      |
c +-------------------------------------------------------+
c m# isotope  percent  &(newline)     $comment
C  m1    1000 2 8000 1 plib 12p elib 03e
  m1   30000 .45  16000 .45 47000 .10 plib 14p elib 01e &
       $ZnS:Ag 2.5 g/cc
C  m2    1000 2 8000 1 plib 12p elib 03e
  m2    8016 .3   7014 .7 plib 14p elib 01e    $air 0.00129
C  m4    1000 2 8000 1 plib 12p elib 03e
  m4   49000 .25 31000 .25 15000 .5 plib 14p elib 01e &
      $InGaP 4.6 g/cc
  m5    49000 .25 31000 .25 15000 .5 plib 14p elib 01e
c  m5    8016 .67 14028 .33 plib 14p elib 01e    $SiO2
c  m1   30000 .5  16000 .5            $ZnS 2.5 g/cc
c  m2    8000 .3   7000  0.7          $air 0.00129 g/cc
c  m4   49000 .25 31000 .25 15000 .5   $InGaP 4.6 g/cc
c  m0 elib plib alib
c
c +-------------------------------------------------------+
c |                   Source Definition                   |
c +-------------------------------------------------------+
 sdef  erg=4.5 par=A   pos=0 0 -.0001    &
      dir=1  rad=d1 vec=0 0 1
 si1 0 0.0001
 sp1 -21 0
c  sdef          &
c  dir=1      &
c  rad=d1     &
c  erg=d2      &
c  vec=0 0 1  par=e      &
c  pos=0 0 .00135
c  si1 0 0.0005
c  sp1 -21 0
c  si2 0 0.01005 0.010553 0.011055 0.011558 0.01206 0.012563 0.013065 &
c      0.013568 0.01407 0.014573 0.015075 0.015578 0.01608 0.016583 &
c      0.017085 0.017588 0.01809 0.018593 0.019095 0.019598 0.020101 &
c      0.020603 0.021106 0.021608 0.022111 0.022613 0.023116 0.023618 &
c      0.024121 0.024623 0.025126
c  sp2 0 1.65341 0.0832472 0.0486526 0.0399384 0.040316 0.0408701 0.0419411 &
c      0.0463593 0.0488002 0.0490574 0.0523356 0.056246 0.0551636 0.0578621 &
c      0.0626941 0.066089 0.0678799 0.0699206 0.0684393 0.0825667 0.0518124 &
c      0.00100239 1.65341 0.0832472 0.0486526 0.0399384 0.040316 0.0408701 &
c     0.0419411 0.0463593 0.0488002
```

```
c
c +-------------------------------------------------------+
c |                   Data Cards                          |
c +-------------------------------------------------------+
c mode N H D T S A P E
  mode  P E A
  DBCN 17J 2
c PHYS:E 100 0 0 0 0 1 1 1 1 0 0 J J 0.917 0.001 0
c  PHYS:E 100 0 0 0 0 1 1 1 1 0 0 1 J 0.917 0.00002
  PHYS:E 14J 1.0e-5
c PHYS:? 100 3J 0 5J          0 0 0 0.917 J 0 0
  PHYS:A  10 3J 0 J 1 0.65 2J 0 0 0 0.917 J J 1e-3
  PHYS:P  100 0 0 0 0 J 0
c  PHYS:P  10 0 0 1 0 J 0
  cut:E j 1.0e-5 $1keV
  cut:P j 1.0e-6 $1keV
  cut:A j 1e-3
nps 400000
c ptrac nps=100 type=a file=asc event=bnk,sur,col,ter,cap
c
c +-------------------------------------------------------+
c |                   LCA Card                            |
c +-------------------------------------------------------+
c LCA 2j 1 6j 0 0
c
c +-------------------------------------------------------+
c |                    Tallies                            |
c +-------------------------------------------------------+
c
c
fc4 alpha flux averaged over the cell in particles/cm^2
 f4:a 1 2 3 4 5 6 7 8 9
 e4 0 198i 5
fc14 alpha flux averaged over the cell in particles/cm^2
 f14:a 10 11 12 13 14 15 16 17
 e14 0 198i 5
fc6 alpha energy deposition averaged over the cell in MeV/g
 f6:a 1 2 3 4 5 6 7 8 9
 e6 0 198i 5
fc16 alpha energy deposition averaged over the cell in MeV/g
 f16:a 10 11 12 13 14 15 16 17
 e16 0 198i 5
fc24 electron flux averaged over the cell in particles/cm^2
 f24:e 1 2 3 4 5 6 7 8 9
 e24 0 198i 0.005
fc34 electron flux averaged over the cell in particles/cm^2
 f34:e 10 11 12 13 14 15 16 17 18
 e34 0 198i 0.005
fc26 electron energy deposition averaged over the cell in MeV/g
 f26:e 1 2 3 4 5 6 7 8 9
 e26 0 198i 0.005
fc36 electron energy deposition averaged over the cell in MeV/g
 f36:e 10 11 12 13 14 15 16 17 18
 e36 0 198i 0.005
fc44 photon flux averaged over the cell in particles/cm^2
 f44:p 1 2 3 4 5 6 7 8 9 10 11 12 13 14 15 16 17 18
```

```
 e44 .00000001 198log .000010
fc46 photon energy deposition averaged over the cell in MeV/g
 f46:p 1 2 3 4 5 6 7 8 9 10 11 12 13 14 15 16 17 18
 e46 .00000001 198log .000010
c
c +-------------------------------------------------------+
c |                    Mesh                               |
c +-------------------------------------------------------+
c
tmesh
c
c (a)radial meshes (b)zaxis(symmetry) (c)angles counterclockwise
c
c  flux=#/cm2     $dose=rem/hr    $pedep=MeV/cm3
c
c flux: flux
c pedep: total energy deposition/unit vol
c dose: dose over cross planes
c
rmesh21:a  flux pedep
c first layer area
cora21    -.0015  158i .0015
corb21    -.0015  198i .0015
corc21    -.0010       .0050
c
rmesh31:a  flux pedep
c first layer area
cora31    -.0015      .0015
corb31    -.0015 158i .0015
corc31    -.0010 198i .0050
c
rmesh41:e  flux pedep
c first layer area
cora41    -.0015  158i .0015
corb41    -.0015  198i .0015
corc41    -.0010       .0050
c
rmesh51:e  flux pedep
c first layer area
cora51    -.0015      .0015
corb51    -.0015 158i .0015
corc51    -.0010 198i .0050
c
rmesh61:p  flux pedep
c first layer area
cora61    -.0015  158i .0015
corb61    -.0015  198i .0015
corc61    -.0010 .0010
c
rmesh71:p  flux pedep
c first layer area
cora71    -.0015      .0015
corb71    -.0015 158i .0015
corc71    -.0010 198i .0010
endmd
c use nps 50 for nbm
```

```
c mplot freq 5 plot ba 1 0 0 0 0 1 ex 50 &
c       la 0 1 tal1 color on la 0 0 pause
c mplot freq 10000 plot ba 1 0 0 0 0 1 ex 50 &
c       la 0 1 tal21 color on la 0 0 pause
```

List of Symbols, Abbreviations, and Acronyms

Ag	silver
Al	aluminum
AMU	atomic mass unit
APG	Aberdeen Proving Ground
APV	alpha-photovoltaic
ARL	Army Research Laboratory
Cu	copper
DEVCOM	US Army Combat Capabilities Development Command
Dy	eysprosium
EM	electromagnetic
Eu	europium
FF	fill factor
FOM	figure of merit
Ge	germanium
I_{SC}	short-circuit current
InGaP	indium gallium phosphide
IPA	isopropyl alcohol
IR	infrared
LED	light-emitting diode
LET	linear energy transfer
MCNP	Monte Carlo N-Particle
MD	molecular dynamics
MeV	megaelectron volt
MPP	maximum power point
ND	neutral density
NRT	Norgett, Robinson, and Torrens

PCB	printed circuit board
PS	polystyrene binder
PV	photovoltaics
$SrAl_2O_4$	strontium aluminate
Si	silicon
SiC	silicon carbide
SRIM	Stopping and Range of Ions in Matter
TJ	triple-junction
UV	ultraviolet
ZnS	zinc sulfide

1 (PDF)	DEFENSE TECHNICAL INFORMATION CTR DTIC OCA
1 (PDF)	DEVCOM ARL FCDD RLB CI TECH LIB
7 (PDF)	DEVCOM ARL FCDD RLA C M WRABACK FCDD RLA GA N BARBIERI FCDD RLA GC M LITZ V PARAMESHWARAN FCDD RLA MF JD DEMAREE FCDD RLA LE L LARKIN J SMITH